Localized Surface Modification of High Strength Aluminum Alloys using Cold Spraying and Friction Stir Processing

by

Wania Jibran

A thesis submitted in partial fulfillment of the requirements for the degree of

Master of Science

Department of Mechanical Engineering
University of Alberta

ABSTRACT

Dimensional restoration and repair methodologies for cold-worked aluminum (Al) alloys are very limited due to strength degradation that occurs during heat application in the process. For example, friction stir processing (FSP) is a well-documented repair methodology for various alloys, but it causes recrystallization in the microstructure of cold-worked Al alloys, negatively affecting their mechanical properties. This study presents a novel approach for surface repairs of high-strength Al alloys without negatively affecting the material strength. Low-pressure cold gas dynamic spraying (150 psig) was used to fabricate aluminum-alumina (Al-Al_2O_3) metal matrix composite (MMC) overlays, hereafter referred to as coatings, on aluminum alloy (AA) 5052-H32, a commonly used cold worked Al grade. The coatings were fabricated from custom mechanical powder blends with varying concentrations of the Al and Al_2O_3 powder, up to a maximum of 75 wt.% Al_2O_3. The coatings (~2.5 mm thick) were then friction stir processed (FSPed) using a cylindrical tool with rotational and traverse speeds of 1200 RPM and 9 mm/s, respectively. Optical microscopy, scanning electron microscopy (SEM), and image analysis were conducted to quantify the Al_2O_3 content in the coatings and analyze the difference in microstructure between the as-sprayed and post-FSPed coating samples. Vickers hardness, abrasion and tensile testing were performed on both the as-sprayed and post-FSPed coatings. The Al_2O_3 content in the metal matrix of the coating increased as the Al_2O_3 content in the powder blend increased, producing a maximum of 35 wt.% Al_2O_3 in the coating fabricated from the powder blend containing 75 wt.% Al_2O_3. FSP increased the uniform distribution of Al_2O_3 in the coating matrix, reduced the porosity in the coating, improved matrix-reinforcement due to ceramic particles and improved interparticle bonding that favorably impacted the coating performance compared to as-sprayed coatings. The post-FSPed coating with 35 wt.% Al_2O_3 exhibited a 22% increase in hardness over bulk AA 5052-

H32. The increase in hardness was attributed to the decrease in mean free path between the Al_2O_3 particles following FSP. Post-FSPed coatings also exhibited lower wear rates compared to the as-sprayed coatings. Significant improvement of the tensile properties was observed after FSP, with the 35 wt.% Al_2O_3 coating having the highest ultimate tensile strength at 172 MPa. The coating elongation and toughness also increased by an order of magnitude following FSP for all coating samples. The post-FSP coating with 5 wt.% Al_2O_3 exhibited the highest elongation of 7% and toughness of 8 J/mm^3. The improved strength of the coatings following FSP was attributed to the improved distribution and dispersion of Al_2O_3 particles in the matrix following FSP. The enhanced ductility of the post-FSPed coatings was attributed to grain refinement that occurs due to dynamic recrystallization from FSP. The results from this study indicated that the microstructural refinement due to FSP significantly enhanced the mechanical performance of cold sprayed coatings. Therefore, it can be concluded that hybridization of low-pressure cold spray with FSP to produce Al-Al_2O_3 coatings can be an effective method for dimensional restoration of high-strength aluminum alloys with high potential also for functional performance.

ACKNOWLEDGEMENTS

I would like to start with thanking my supervisors, Dr. André McDonald and Dr. Priti Wanjara. Without their support and guidance during my graduate studies this thesis would not be possible. Having done my degree in unprecedented times due to Covid-19, their support and understanding was elemental for my experience. I would also like to thank Dr. Javad Gholipour Baradari from the National Research Council of Canada's Aerospace Research Centre (NRC-ARC) for his support and encouragement through my thesis. His insight and fruitful discussions allowed me to gain more from my experience, academically and professionally. It has been an enjoyable 2 years and I have grown immensely both personally and professionally. I have the three of them to thank for that. I would also like to thank Dr. James Hogan for being so generous with his support and allowing me to use his lab. I would also like to thank him for making my experience of graduate courses very rewarding. Discussions with him have also allowed me to grow professionally.

I would also like to thank everyone who assisted me with the technical work through my project. I would like to start by Mr. Shahed Taghian Dehaghani for his assistance in familiarizing me with the thermal spray shop and spraying processes. I would like to thank Mr. Kapil Bhagavathula for training me to the use hardness testing machine and digital image correlation. I am also grateful for our discussions through these two years, which have been immensely helpful in navigating graduate studies. I would like to thank Dr. Chenwei Shao for assisting me with the SEM imaging for my samples and several fruitful discussions.

I would also like to thank everyone in the MecE workshop for assisting me during my graduate studies. In particular, I would like to thank Mr. Daniel Mooney and Mr. David Parlin for

assisting me with wire EDM for my coating samples. I would also like to thank Mr. Mitul Patel for his assistance with the tensile testing for my project. I would like to thank Mr. Maxime Guerin from the NRC-ARC for his assistance with the FSP.

I would like to thank my friends and family for always being there for me and supporting me through the way. In particular, I would like to thank Kelsea Sterling, Badar Zahoor and Ali Tariq Shaikh for staying by my side and having faith in me, despite my demanding schedule. I would like to thank my sister, Zinnia Jibran, for bringing much needed comic relief into my days. Lastly, I would like to thank my parents for their unwavering support and love, which has motivated me to complete my work. I would like to thank them for being supportive of my decisions and encouraging me for as long as I can remember. Without all these people, I would not be the person I am today, so to them I am eternally grateful.

CONTENTS

Abstract ii

Acknowledgements iv

Contents vi

List of Tables ix

List of Figures x

Nomenclature xiii

Greek Symbols xiii

Subscripts xiv

1. Introduction 1

1.1. Repair Methodologies for High Strength Al Alloys 1

1.2. Friction Stir Processing 2

1.3. Cold Spraying 4

1.4. Motivation 6

1.5. Objectives 7

1.6. Thesis Organization 8

2. Background 9

2.1. Mechanical Properties of Cold Sprayed MMC Coatings 9

2.2. MMC coatings for Repairs of AA 5052-H32 12

3. Experimental Methods 16

3.1. Feedstock Powder and Substrate 16
3.2. Cold Spray Deposition 18
3.3. Friction Stir Processing 20
3.4. Characterization and Microstructural Analysis 22
3.5. Micro-hardness 23
3.6. Dry Abrasion Testing 24
3.7. High Stress Abrasion Testing 25
3.8. Strain Measurements using Digital Image Correlation 27
3.9. Tensile Testing 29
4. Results and Discussion 30
4.1. Coating Characterization 30
4.2. Mechanical Performance 37
4.2.1. Coating hardness 37
4.2.2. Coating-Substrate Interface Hardness 40
4.3. Mechanical performance and properties 42
4.4. Fracture Surfaces 52
4.5. Strengthening mechanisms 56
4.6. Abrasion performance 60
5. Conclusion 65
6. Future Work and Recommendations 68

References 72

Appendix A – Stress Strain Curves 82

LIST OF TABLES

Table 1: Process parameters used for the cold spray deposition..... 18

Table 2: Al_2O_3 particle size in the coating for both as-sprayed and post-FSPed coatings. 34

Table 3: Al_2O_3 content, Young's modulus, ultimate tensile strength, toughness and failure strain for as-sprayed and post-FSPed coatings. 48

LIST OF FIGURES

Figure 1: Schematic of a typical friction stir process [9]. 3

Figure 2: Schematic for a typical cold spray process [24]. 5

Figure 3: SEM image of the aluminum powder morphology. 17

Figure 4: SEM image of the alumina powder morphology. 17

Figure 5: The cold spray gun mounted on the HP-20 Motoman robot [44]. 19

Figure 6: Schematic of FSP performed for Al-Al_2O_3 MMC coatings [20]..... 20

Figure 7: Friction stir processing experimental setup [45]. 21

Figure 8: Schematic of the dry abrasion test assembly as per ASTM G65 [47]..... 25

Figure 9: Schematic of test assembly for high stress abrasion testing as per ASTM B611 [48]. 26

Figure 10: Image presenting (a) the surface along the reduced section of the gauge length of the tensile specimen. (b) Image showing the AOI for which the average axial strains were calculated. 28

Figure 11: Tensile test assembly coupled with the DIC camera setup. 29

Figure 12: SEM images of the coating cross-sections of the as-sprayed coatings with (a) 5 wt.% Al_2O_3, (b) 23 wt.% Al_2O_3, (c) 35 wt.% Al_2O_3. 31

Figure 13: Graph of Al_2O_3 content in the powder blend versus that in the coating. 32

Figure 14: SEM images of the coating cross-sections of the post-FSPed coatings with (a) 5wt.% Al_2O_3, (b) 23 wt.% Al_2O_3, (c) 35 wt.% Al_2O_3. 33

Figure 15: Images of the coating cross-sections for as-sprayed coatings (a) 5 wt.% Al_2O_3 (b) 23 wt.% Al_2O_3 and post-FSPed (c) 5 wt.% Al_2O_3 (d) 23 wt.% Al_2O_3..... 34

Figure 16: Mean free path between the Al_2O_3 particles versus the Al_2O_3 content in the coating. 35

Figure 17: Coating porosity versus the Al_2O_3 content in the coating. 35

Figure 18: Relationship between coating hardness and Al_2O_3 content. 39

Figure 19: Relationship between the mean free path between Al_2O_3 particles and coating hardness. 39

Figure 20: Hardness map tracking the hardness changes between the substrate, interface and coating for the post-FSP samples for 5 wt.% Al_2O_3 and 35 wt.% Al_2O_3 samples. The coating cross-section image is for the post-FSPed coating with 35 wt.% Al_2O_3 and is only displayed to indicate the indent location. 42

Figure 21: Average tensile stress versus tensile strain for (a) as-sprayed and (b) post-FSPed coatings. The legend indicates the wt.% Al_2O_3 for each sample. 49

Figure 22: Relationship between ultimate tensile strength and Al_2O_3 content for as-sprayed and post-FSPed coatings. 50

Figure 23: Relationship between coating toughness and Al_2O_3 content for as-sprayed and post-FSPed coatings. 50

Figure 24: Relationship between failure strain and Al_2O_3 content for as-sprayed and post-FSPed coatings. 51

Figure 25: Images of the fracture of tensile samples for as-sprayed coatings with (a) pure Al, (b) 5 wt.% Al_2O_3, (c) 23 wt.% Al_2O_3, (d) 35 wt.% Al_2O_3 and post-FSPed coating with (e) pure Al, (f) 5 wt.% Al_2O_3, (g) 23 wt.% Al_2O_3, (h) 35 wt.% Al_2O_3. 54

Figure 26: SEM images of the tensile fracture surfaces for as-sprayed coatings with (a) pure Al, (b) 5 wt.% Al_2O_3, (c) 23 wt.% Al_2O_3, (d) 35 wt.% Al_2O_3 and post-FSPed coating with (e) pure Al, (f) 5 wt.% Al_2O_3, (g) 23 wt.% Al_2O_3, (h) 35 wt.% Al_2O_3. 55

Figure 27: Dry abrasion wear rate versus Al_2O_3 content for as-sprayed and post-FSP coatings. 63

Figure 28: High stress abrasion wear rate versus Al_2O_3 content for as-sprayed and post-FSP coatings. 64

Figure 29: Preliminary adhesion testing as per ASTM C633 for the as-sprayed coatings. On the figure, C indicates cohesive failure in the coating and E indicates failure in the epoxy section. 69

NOMENCLATURE

d	distance between dislocation [μm]
k	material coefficient
N	number of particle intersects per unit length $\left[\frac{1}{\mu m}\right]$
P	applied force [N]
s	sliding distance [m]
v	volume fraction
V	volume of arbitrary body [mm^3]
W	wear rate $\left[\frac{mm^3}{Nm}\right]$

Greek Symbols

ε	strain $\left[\frac{mm}{mm}\right]$
ρ	dislocation density $\left[\frac{1}{mm^2}\right]$
λ	mean free path [μm]
σ	stress [Pa]
φ	particle size [μm^2]

Subscripts

r	reinforcing phase
L	per unit length
FS	flow stress
YS	yield stress
OR	Orowan
HP	Hall-Petch

1. INTRODUCTION

1.1. Repair Methodologies for High Strength Al Alloys

Aluminum (Al) alloys can be classified into two categories: heat treatable and non-heat treatable. The repair methodologies that exist for these alloys are limited or non-existent currently as they often introduce strength losses in the material, which prevent return to service. Considering existing repair methodologies based on fusion technologies, the high temperatures and heat input during the repair process negatively affect the mechanical properties of the material [1]. For instance, heat treatable Al alloys, such as the 2xxx, 6xxx or 7xxx series, are strengthened by precipitation hardening. When exposed to high heat for a specific amount of time during a repair process, the material experiences microstructural changes such as precipitate dissolution, which leads to significant strength losses in the material [2-3]. To some extent, solution annealing followed by aging can be used to recover the strength of repaired 2xxx or 7xxx series parts, but such heat treatments can lead to part distortion that must remain within acceptable/tolerable limits specified for return to service. By contrast, non-heat treatable Al alloys, such as the 5xxx series, are strengthened by work-hardening to enhance their mechanical properties. Heat application to a work-hardened Al alloy causes the material to return to its annealed condition, reducing the strength significantly [1, 4]. It is due to these reasons that repairs of high strength, cold worked Al alloys remains a longstanding challenge, and presently these alloys are considered unrepairable. However, developing repair methodologies for cold worked Al alloys is essential, as these alloys are frequently used in marine applications, building and construction and to make pressure vessels due to their excellent corrosion properties. They are also frequently used in aerospace and automotive applications due to their high strength and low weight, as well as in the defence sector

for military vehicles due to their high strength and good weldability. Considering the diverse and broad application of cold worked Al grades, an effective repair methodology would provide game changing advantages to industry.

1.2. Friction Stir Processing

As a derivative of friction stir welding (FSW), friction stir processing (FSP) is a solid-state, surface modification process used to modify microstructural and mechanical properties of metals [5-6]. It is often used to repair surface cracks and reduce casting porosity [4]. During this process, a rotating cylindrical tool with a larger diameter shoulder and smaller diameter pin (relative to FSW), is plunged into the material and then traversed along the work piece surface (see Figure 1). The tool exerts a downward force onto the material, which generates frictional heat and softens the material under the shoulder, while the rotation of the tool inside the material subjects the material to severe plastic deformation at high strain rates [5-6]. This thermoplastic deformation can reduce and repair defects such as cracks and pores. FSP can also improve the mechanical and microstructural properties of metals [7-8]. It has been reported that FSP causes grain refinement and creates high angle grain boundaries, which result in improved ductility in materials [4]. FSP also improves the strength, ductility and fatigue properties of cast materials by breaking up the dendritic microstructure and creating refined uniaxial grains [4]. Since FSP is a solid-state process, it has the added benefit of not introducing as many metallurgical changes to the material as would be expected in traditional welding processes. Therefore, FSP is an attractive technology for improving and repairing metals and alloys.

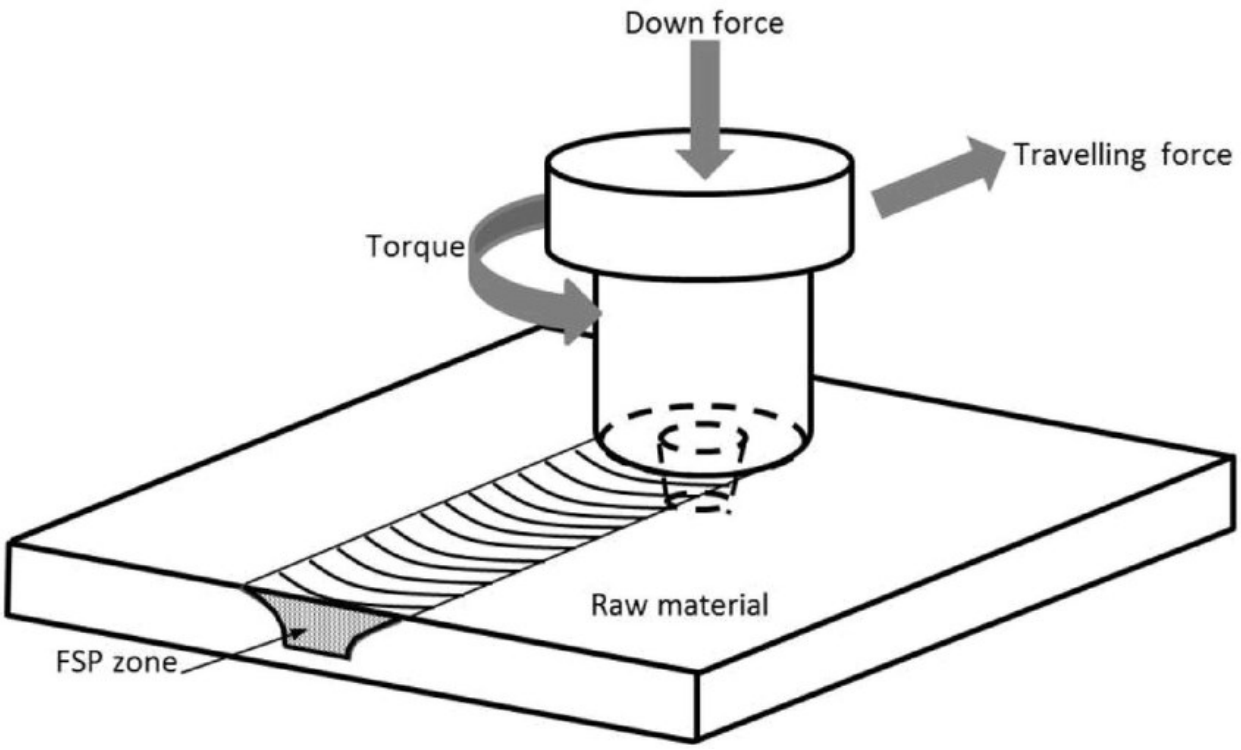

Figure 1: Schematic of a typical friction stir process [9].

For repairs and refurbishment of high strength Al alloys, especially the 2xxx, 6xxx and 7xxx series, FSP is a good candidate due to its lower heat input compared to other welding processes. However, despite the lower heat input conditions, FSP still causes strength degradation in high strength Al alloys due to precipitate dissolution for heat treatable grades (2xxx, 6xxx and 7xxx series), as well as dynamic recovery and recrystallization in cold-worked materials [1]. Therefore, traditional FSP is not an effective repair methodology, especially for repairing cold worked Al alloys. In an effort to remedy the reduction in strength, inclusion of ceramic particles into the material was explored [4]. Nolting *et al.* [4] found that by introducing Al_2O_3 particles into AA 5083 and then dispersing the ceramic particles into the alloy through FSP compensated for the strength losses during FSP. This was accomplished by cutting several grooves into the base plate,

introducing the ceramic particles and then traversing the FSP tool over the surface to disperse the ceramic particles into the base material [4]. Though this approach improved the hardness and yield strength of the repair section compared to the parent material, it came with a penalty of 50% to the ductility of the repaired section [4]. Nonetheless, this technique and study presented the first viable approach for repairs of seemingly unrepairable cold worked Al alloys, even though the heat input during the multiple FSP passes required for densification and adequate distribution of the reinforcement particles led to softening of the underlying substrate. Another limitation of the method proposed by Nolting *et al*. [4] was in the method of introducing ceramic particles into the material during FSP, which was a difficult process requiring several steps to ensure good dispersion of the ceramic particles and good compaction of the ceramic particles in the grooves in the plate. Therefore, addressing these limitations represent key objectives to further developing an efficient and effective repair methodology that would also not compromise the mechanical performance of high strength, cold worked Al alloys.

1.3. Cold Spraying

Cold spraying is a solid-state coating fabrication technology used to produce dense metal or metal matrix composite (MMC) coatings. During cold spraying, powder particles are accelerated to supersonic velocities using a carrier gas through a de Laval nozzle, as illustrated in Figure 2. The powder particles attain high kinetic energy as they exit the nozzle, which causes them to undergo severe plastic deformation upon impact with the substrate. This enhances adhesion with the substrate [7, 10–16]. Successive deposition of particles creates layers that produce a coating on the substrate. As implied by the name, cold spraying is a cold deposition process (0-700°C) [17] as compared to other thermal spray processes. Cold spray processes always operate at temperatures

that are lower than the melting point of the feedstock powder. Therefore, the coatings fabricated using cold spraying are nearly devoid of oxidation, decarburization, metallurgical changes, and residual thermal stresses [11, 17–19]. Cold sprayed coatings are frequently used in the industry for surface modification applications to improve wear performance and hardness of surfaces [16, 20, 21]. Since it is a solid-state deposition process, the interparticle bonding is most likely due to the mechanical interlocking of particles in the coating. Therefore, cold sprayed coatings exhibit brittle behaviour under tensile loading as there is weak interparticle bonding in comparison to other coating and additive manufacturing processes [6]. Cold spraying is divided into two types: high-pressure and low pressure. While high-pressure cold spraying can deposit coatings of the same thickness quicker compared to a low-pressure system, the low-pressure system has certain advantages. Low-pressure cold spraying is less expensive compared to high-pressure cold spraying and creates less noise pollution during operation. Low-pressure cold spraying can also be performed in-situ for field repairs. Cold sprayed coatings are used for various corrosion and wear protection applications in the oil/gas, automotive and aerospace industries [22-23].

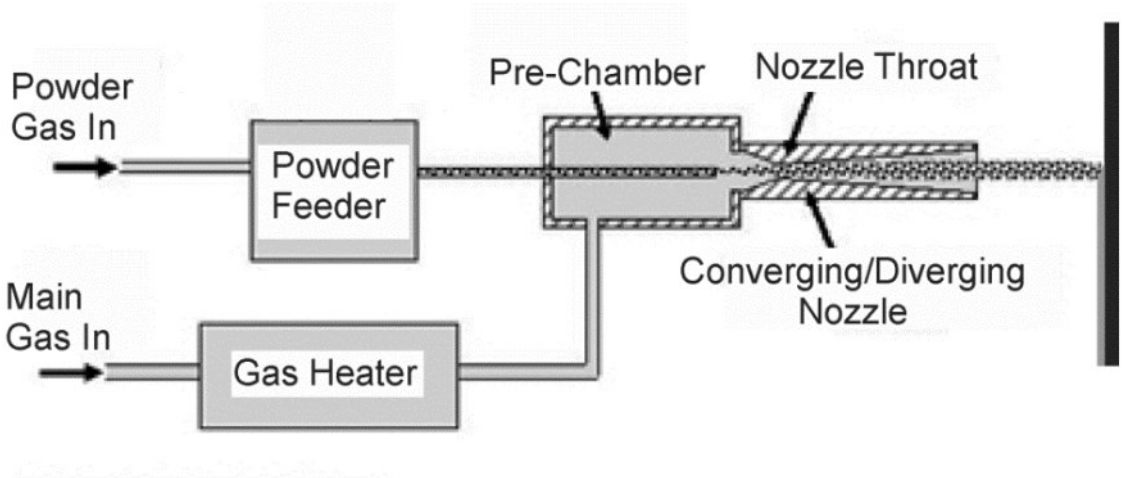

Figure 2: Schematic for a typical cold spray process [24].

1.4. Motivation

Considering unrepairable high strength Al alloys as motivation, this study presents a repair methodology for AA 5052-H32, which is a cold worked, unrepairable Al alloy. A cold spray-FSP hybrid approach is suggested in this study to develop Al-Al_2O_3 MMC coatings with improved mechanical properties to be used for surface modifications and repairs for AA 5052-H32. Ceramic particle inclusion during FSP has been explored as a repair methodology for Al alloys, which resulted in improved hardness and tensile strength [4]; however, the method included several steps and resulted in overall material softening as the tool penetrated below the base metal surface. Therefore, coupling FSP with a cold sprayed coating is being explored to reduce the manufacturing complexity associated with introducing the ceramic particles, eliminating the base material softening as well as the loss of material from the top surface after FSP. Cold sprayed coatings have been used extensively for surface modifications in the oil and gas, automotive and aerospace industry, for wear and corrosion prevention applications [10, 17, 25]. A thorough understanding of the characterization of these coatings is somewhat limited to localized testing systems such as hardness testing [20]. Researchers have also explored the wear performance of cold sprayed MMC coatings to improve wear performance of parts in commission [25]. However, limited research exists for full field testing of cold sprayed coatings, such as tensile testing. Similarly, very limited research exists for full scale testing of cold sprayed and FSPed coatings to analyze their mechanical performance. Some researchers have analyzed the effect of FSP on the coating hardness and wear [20, 26]; however very few studies have been conducted that explore mechanical properties such as tensile strength, toughness, elongation, and quantify fracture behaviour of cold-sprayed coatings followed by FSP. Conducting full field testing to quantify the mechanical properties of cold sprayed coatings before and after FSP can also elucidate the possibility of doing functional repairs

of alloys in addition to surface repairs by creating coating deposits that match the material properties of the base substrate.

1.5. Objectives

The goal of this research was to develop a cold spray-FSPed hybrid repair methodology for (presently) unrepairable Al alloys. This study explores the changes in the microstructural and mechanical properties of cold sprayed Al-Al_2O_3 coatings after FSP. The specific objectives of the study were to:

1. Fabricate low-pressure cold sprayed coatings with Al and varying content of Al_2O_3 wt.% and conduct FSP on the coatings.
2. Analyze the microstructural changes between the as-sprayed and post-FSPed coating samples by conducting optical microscopy (OM) and scanning electron microscopy (SEM).
3. Determine mechanical properties by conducting hardness tests and uniaxial tensile tests.
4. Explore and analyze the use of the digital image correlation technique in the mechanical testing of cold sprayed coatings.
5. Determine the wear/erosion performance of the as-sprayed and post-FSPed coatings by performing abrasion testing.
6. Study the effect of reinforcing particle content on the mechanical properties of the as-sprayed and post-FSPed coatings.

7. Analyze the effects of changing microstructure due to FSP on the mechanical properties of the coatings.
8. Analyze the stress-strain behaviour for both the as-sprayed coatings and post-FSPed coatings.
9. Compare the properties of the post-FSPed coatings with bulk AA5052-H32 to determine feasibility of repair.
10. Analyze the fracture behaviour of the as-sprayed and post-FSPed coatings to determine the modes of fracture.

1.6. Thesis Organization

This thesis document is divided into several chapters. Chapter 2 describes the current state of research on cold sprayed MMC coatings and MMC coating repairs for AA5052-H32. Chapter 3 describes the experimental methods used to fabricate and characterize the cold-sprayed and FSPed Al-Al_2O_3 MMC coatings. Chapter 4 presents the results and discussion of the experimental data on the performance and properties of the coatings. Chapter 5 presents the conclusions of this thesis, while Chapter 6 discusses recommendations for future work stemming from the findings of this thesis.

2. BACKGROUND

2.1. Mechanical Properties of Cold Sprayed MMC Coatings

MMC coatings have recently generated interest in the engineering industry due to their improved hardness and erosion properties over bulk materials. The mechanical properties of cold sprayed metal coatings can be improved in hardness and erosion performance by incorporating ceramic reinforcing particle to fabricate cold sprayed MMC coatings [16]. This is accomplished by co-depositing a ductile metal powder with a hard, reinforcing phase such as a carbide or oxide. The ductile metal powders are mechanically mixed with the hard, reinforcing powder in the desired composition and the MMC mixture is then deposited using cold spray.

It has been established that physical defects such as porosity can have significant negative effects on the mechanical properties of cold sprayed coatings [16]. Often for coatings, it is found that physical defects such as porosity accelerate failure under loaded conditions as pores can be sites for micro void nucleation and crack propagation. Therefore, coatings that are porous will exhibit poor tensile behaviour and will fail at lower loads. Since cold spraying is a solid state deposition process, mechanical interlocking is the dominant bonding mechanism in the coating [20]. Feedstock metal powders such as Al have low densities and often also have irregular morphologies. This causes air entrapment between particle splats during the cold spray deposition process, which creates pores in the Al coating [20]. Researchers have found that this porosity can significantly impact the mechanical performance of cold sprayed metal coatings [10, 27, 28]. The incorporation of ceramic particles to deposit cold sprayed MMC coatings has been found to reduce coating porosity, thereby improving hardness, wear and corrosion performance [10, 27, 28]. For instance, Spencer et *al.* [28] observed accelerated corrosion for cold sprayed coatings that were

not sufficiently dense, and lowering the porosity in the coatings yielded improved corrosion resistance. Loganathan *et al.* [29] found the tribological performance of cold sprayed Al-Nano Diamond MMC coatings to improve significantly as the coating porosity reduced to ~1% following heat treatment. Vaz *et al*. [30] used various thermal spray processes to fabricate coatings and compare the corrosion and wear performance; they found that cold spraying yielded the lowest porosity in the coatings as well as enhanced corrosion and wear performance. Similarly Zhao *et al.* [31] compared the corrosion and wear performance of NiCrAl coatings deposited using plasma spraying and cold spraying; their results indicated that the cold sprayed coatings had lower porosity and a more compact mechanically mixed layer structure, which also yielded improved wear and corrosion performance compared to the plasma sprayed coating. Therefore, porosity plays a key role in the improvement of the mechanical properties of cold sprayed coatings.

MMC coatings with reinforcing ceramic material not only reduce porosity, but also improve mechanical performance of materials by enhancing coating reinforcement. Researchers have found that incorporating alumina (Al_2O_3) particles to Al powder produces cold sprayed MMC coatings that exhibit higher hardness compared to pure Al cold sprayed coatings [20, 28, 32]. Hodder *et al*. [20] found that the hardness increased from ~50 HV for the pure Al cold sprayed coating to ~85 HV for the Al-Al_2O_3 MMC coating containing 48 wt.% Al_2O_3. Spencer *et al*. [28] found that the wear rate of Al-Al_2O_3 MMC coating containing 30 vol.% Al_2O_3 decreased significantly compared to a pure Al cold sprayed coating. The improved mechanical properties of MMC coatings compared to metal coatings has been attributed to the coating microstructure and strengthening effects of the reinforcing particles. Munday *et al.* [16] concluded that increasing the content of the reinforcing phase in cold sprayed coatings improved coating hardness and tensile strength, as increasing hard particle content reduced the mean free path between reinforcing

particles, increased the interfacial area between the metal matrix and the reinforcing particles, and reduced the reinforcing particle size in the coating. While surface modification applications, such as wear and corrosion protection, are extensively studied for cold sprayed coatings, less research exists on exploring the tensile properties of cold sprayed MMC coatings. Some researchers have studied the tensile properties of pure metal coatings and found the ductility of the coatings to be much lower compared to bulk metals [33, 34]. The biggest drawback of cold sprayed coatings is the poor elongation and ductility of the coating due to weak interparticle bonding and presence of porosity. Munday *et al.* [16] explored the tensile performance of WC-Ni MMC coatings and found a similar response. Full scale testing such as tensile testing for cold sprayed MMC coatings has not been explored as extensively as metal coatings in research.

Due to their enhanced mechanical properties, Al-Al_2O_3 coatings are used to improve surface properties for metals such as magnesium, aluminum and aluminum alloys which are frequently used in the automotive, aerospace, and military defense applications. They prove useful in enhancing the surface hardness and wear resistance in aggressive wear environments. Cold sprayed Al-Al_2O_3 MMC coatings are often preferred over bulk material as it is often more feasible to coat a part in use rather than machining bulk Al or Al alloy. Typically, higher temperature deposition processes such as high velocity oxygen fuel (HVOF) spraying or atmospheric plasma spraying (APS) are used to enhance surface properties [11, 17, 18, 32], however the high temperatures involved in these processes introduce unwanted metallurgical changes and residual stresses in the coating. Therefore, using cold spray to deposit Al-Al_2O_3 MMC coatings is an effective way to remedy these issues. In this study, the effect of reinforcing particles on the mechanical properties of the coatings will be explored and the strengthening mechanisms involved with hard particle reinforcement will be discussed.

2.2. MMC coatings for Repairs of AA 5052-H32

As mentioned in section 2.1, cold sprayed MMC coatings have been explored extensively for surface restoration and modification of various metals, including steels and Al alloys [19, 29–31, 35–38]. Gao *et al.* [38] explored surface modification of steel substrates using high pressure cold sprayed WC MMC coatings to produce surfaces with enhanced hardness. While they were able to achieve surfaces with improved hardness, they found that achieving thick coatings was a challenge using high pressure cold spraying. Similarly, Dosta *et al.* [37] tried to improve the surface wear and corrosion for AA 7075-T6 using high pressure cold sprayed WC MMC coatings and found that the enhanced wear rates came at the compromise of very thin coatings. Therefore, achieving thick MMC coating deposits using high pressure cold spraying is currently a challenge in the industry. This is why it is common for large scale production facilities to only deposit metal coatings using high pressure cold spraying. In order to avoid the issue of thin coatings, low-pressure cold spraying was explored by researchers. Wang *et al* [35] deposited WC MMC coatings using low-pressure cold spraying in order to enhance surface hardness, and were able to achieve thick coating deposits with enhanced surface hardness. Similarly, Spencer *et al.* [19] used low-pressure cold sprayed Al-Al_2O_3 coatings to enhance the surface of a magnesium alloy and were able to successfully modify surface hardness. Loganathan *et al.* [29] explored the addition of nano diamond particles into an Al coating deposited using low-pressure cold spray and found the wear and corrosion resistance of the carbon steel base material to increase significantly. Similarly, MMC coatings have been used to perform surface modifications and repairs for bulk metals such as pure Al and Al alloys for wear and corrosion protection [39–41].

Though extensive research exists on surface modification using cold sprayed MMC coatings for wear and corrosion protection, there is limited research on the mechanical properties of cold sprayed coatings and their potential for functional repairs. Majority of the surface repairs being performed using thermal sprayed coatings consist of geometric repairs. Geometric repairs refer to coatings applied to restore the geometry with no specification for functional properties. Examples of geometric repairs include using coatings to size up shafts, surface repairs to eliminate defects such as scratches and broken edges, and filling holes or minor cavities in larger parts. Often, geometric repairs can be done with different coating material compared to the base material as the homogeneity of repair material and base material is not necessary for geometric repairs. Such inhomogeneous repairs have been especially useful for restoring the geometry of parts damaged by corrosion alongside improvements in corrosion resistance; confusingly, such repairs have at times been referred to as functional for the corrosion resistance functionality that is restored/enhanced by the repair. However, strictly, functional repairs refer to restorations that are functionally equivalent (or superior) in performance (structural, load-bearing, fatigue critical, etc.) to the original material/part.

To this point, cold-worked unrepairable Al alloys, such as AA5052-H32, have functional repair requirements, for which currently there are no effective and efficient repair methodologies. It is important for functional repairs that the properties of the coating be the same (or higher than) and the bulk material, so as to ensure the behaviour of the repaired part is the same as (or better than) the base material under the loaded conditions required for its function. Since high heat input deposition processes can not be used for repairs of cold-worked Al alloys, cold sprayed coatings are an attractive solution due to the lower operational temperatures during spraying that limit the heat input and concomitant damage to the base material. In spite of this advantage, the cold sprayed

coatings are deposited in the solid-state with only mechanical bonding and are, thus, brittle in nature with poor tensile performance. To enhance bonding of cold sprayed coatings, inspiration was drawn from the promising early results of FSP coupled with ceramic particle inclusion for repairing cold-worked Al alloys. In particular, Nolting *et al.* [4] explored repairs of AA5083 using FSP with ceramic particle inclusion and were able to get improved hardness and yield strength in the repaired MMC region of the base material. However, the elongation of the repaired section was lower than that of the base material. Softening of the underlying base material also limited the overall mechanical performance. Thus, in the present research coupling of the cold spray and FSP technologies was deliberated to create synergistic benefits of minimal impact to the cold worked base material combined with the deposition of high-performance coating. To date, very limited research exists on the potential of using cold spraying and FSP, and none of these have been for repairs of unrepairable, cold worked Al alloys. Some researchers have explored the effects of FSP on cold sprayed coatings [6, 26, 42, 43], however the majority of the research has been focused on surface modification applications, such as wear and corrosion protection. Peat *et al.* [26] explored the effects of FSP on wear resistance of cold sprayed WC-Co and Al_2O_3 coatings deposited on stainless steel substrates. They were able to conclude that FSP enhanced the hardness and wear resistance of the MMC coating significantly, which was attributed to the improved distribution of ceramic material in the MMC coating following FSP [26]. Huang *et al.* [42] performed FSP on cold sprayed SiC-AA5056 coating deposited on pure Al substrates to compare the tribological performance of the as-sprayed and FSPed coatings. They were able to conclude that due to the improved ceramic particle distribution, the coefficient of friction for the FSPed coatings was higher than the as-sprayed coatings [42]. Moreover, research on the mechanical performance of FSPed cold sprayed coatings, characterized using full-scale tests such as uniaxial tensile testing,

is further limited. Li *et al*. [43] performed tensile testing for a cold sprayed and FSPed Cu-Zn coating deposited on Cu substrates and found that ultimate tensile strength (UTS) and elongation of the samples experienced increases following FSP. This was attributed to the microstructural changes leading to grain refinement in the coatings [43]. Similarly, Yang *et al.* [6] performed FSP on cold sprayed AA2024-Al_2O_3 coatings deposited on a Cu substrate and found the UTS and elongation to increase following FSP. They attributed the enhancements to the improved ceramic distribution in the coating [6].

Realizing the distinct advantages of both solid-state processes, namely cold spraying and FSP, the inherently cold operational conditions of the former would minimize heat input and microstructural changes to the base material during deposition of the coating; then FSP would bring the advantage of enhancing consolidation, bonding and reinforcement homogeneity of the cold sprayed coating to maximize its performance and functionality. Thus, this research study, explored coupling cold sprayed Al-Al_2O_3 coatings with FSP to understand the feasibility of this hybrid repair methodology to restore geometric and functional characteristics of unrepairable, cold worked AA5052-H32.

3. EXPERIMENTAL METHODS

3.1. Feedstock Powder and Substrate

Several mechanical powder blends were prepared to fabricate the low-pressure cold sprayed Al-Al_2O_3 coatings. The powders used to prepare the mechanical blends included commercially available pure Al powder (SST-A5001, CenterLine, Ltd., Windsor, ON, Canada) and commercially available Al_2O_3 powder (AMDRY 6060, Oerlikon Metco Inc., Westbury, NY, USA) with a size distribution of -45+5 μm (5 to 45 μm). Figure 3 and Figure 4 show the morphology of the Al and Al_2O_3 powder particles, respectively. The Al particles have an irregular shape, while the Al_2O_3 particles appear to have a more angular shape. Four different Al-based mechanical blends were explored in this study with the Al_2O_3 content varying from 0 wt.% to 75 wt.%. The mechanical blends were selected based on previous work by Hodder *et al.* [20] exploring FSP of low-pressure cold sprayed Al-Al_2O_3 coatings.

All the coatings were deposited on AA5052-H32 substrates. AA5052-H32 was selected as the substrate material as it is a high strength aluminum alloy with limited (no) repair methodologies. Since the roughness of the substrate is an important factor for good adhesion between the coating and the substrate [19][32], the substrates were grit-blasted using an alumina-based abrasive (#24 alumina grit, Manus Abrasive Systems Inc., Edmonton, AB, Canada). The abrasive was dispensed towards the substrate by the grit blaster at 90 psi pressure to roughen the surface and promote coating adhesion.

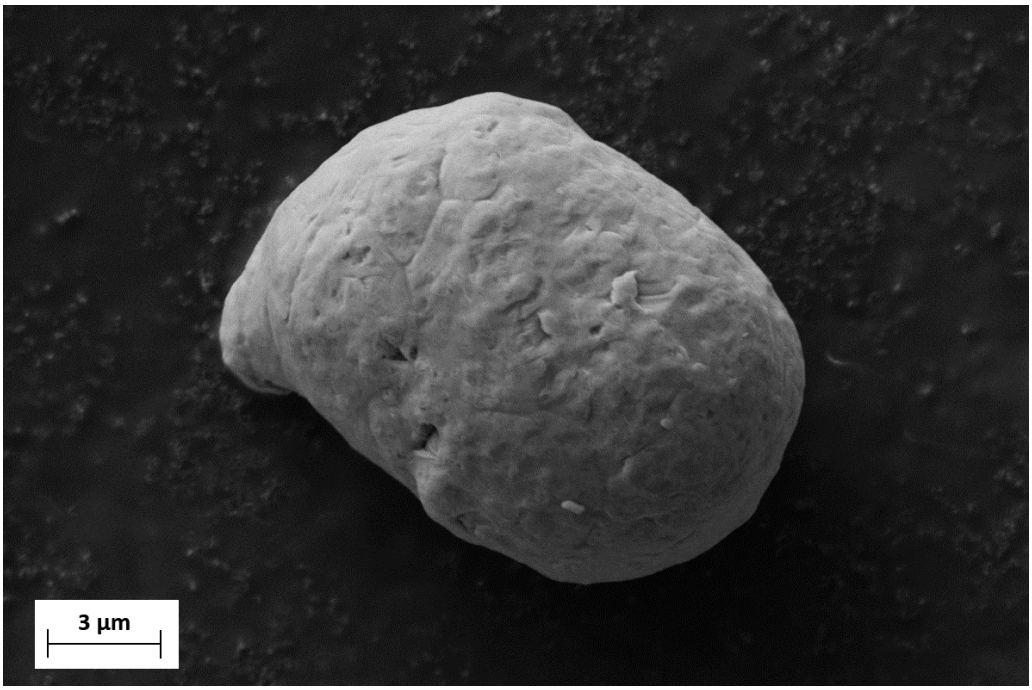

Figure 3: SEM image of the aluminum powder morphology.

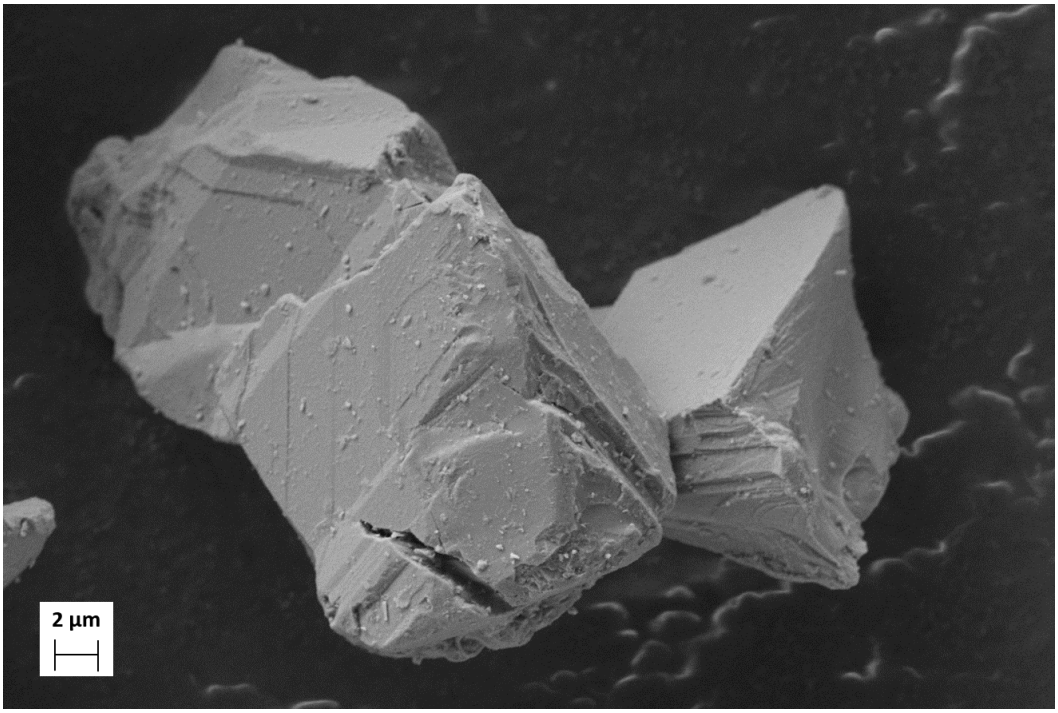

Figure 4: SEM image of the alumina powder morphology.

3.2. Cold Spray Deposition

The coating deposition was carried out using a low-pressure cold spray system (SST series P, CenterLine, Ltd., Windsor, ON, Canada). The cold spray torch was mounted on an automatic robot (HP-20, Motoman, Yaskawa Electric Corp., Waukegan, IL, USA), which allowed for consistent torch manipulation to achieve repeatable coating depositions (see Figure 5). The robot allowed for keeping the nozzle to substrate stand-off distance and torch traverse speed constant. The stand-off distance is the distance between the nozzle and the substrate. The robot was programmed to deposit the coating in a linear direction with fixed increments in the in-plane perpendicular direction after travelling the width of the substrate. Compressed air at 689 KPa was used as the carrier gas for the coating deposition. A nozzle with a length of 120 mm, an entrance diameter of 4.46 mm, and an exit diameter of 6.40 mm was used to transport the powder and the compressed air from the de Laval nozzle to the substrate. The process parameters were optimized to maximize coating thickness and are presented in Table 1.

Table 1: Process parameters used for the cold spray deposition.

Process Parameter	**Value**
Carrier Gas	Compressed Air
Carrier Gas Pressure	689 kPa
Carrier Gas Temperature	300°C
Stand-off Distance	5 mm
Nozzle Velocity	4.5 mm/s

Figure 5: The cold spray gun mounted on the HP-20 Motoman robot [44].

3.3. Friction Stir Processing

FSP was performed on the coated AA5052-H32 substrates after the Al-Al_2O_3 coatings were deposited using low-pressure cold spraying. The coated AA5052-H32 plates were secured to a FSP table and a cylindrical FSP tool of 13 mm diameter with a flat surface was traversed over the coating deposit at constant speed of 9 mm/s. A custom machine equipped with a weld head assembly was used to carry out the FSP, as illustrated in Figure 6 and Figure 7 (ISTIR PDS, MTS Systems Corporation, MN, USA). The rotational speed for the cylindrical tool was set to 1200 rotations per minute (RPM). The tool was plunged into the deposit until the entire tool surface was in contact with the coating. The tool was operated in force control mode; therefore, the axial force was proportional to the penetration depth. The tool was operated with an axial force in a range between 6 kN to 10 kN, depending on the required depth.

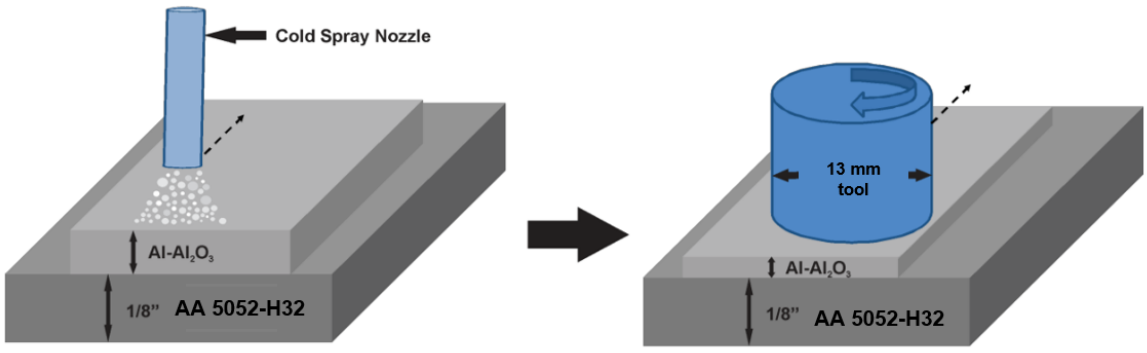

Figure 6: Schematic of FSP performed for Al-Al_2O_3 MMC coatings [20].

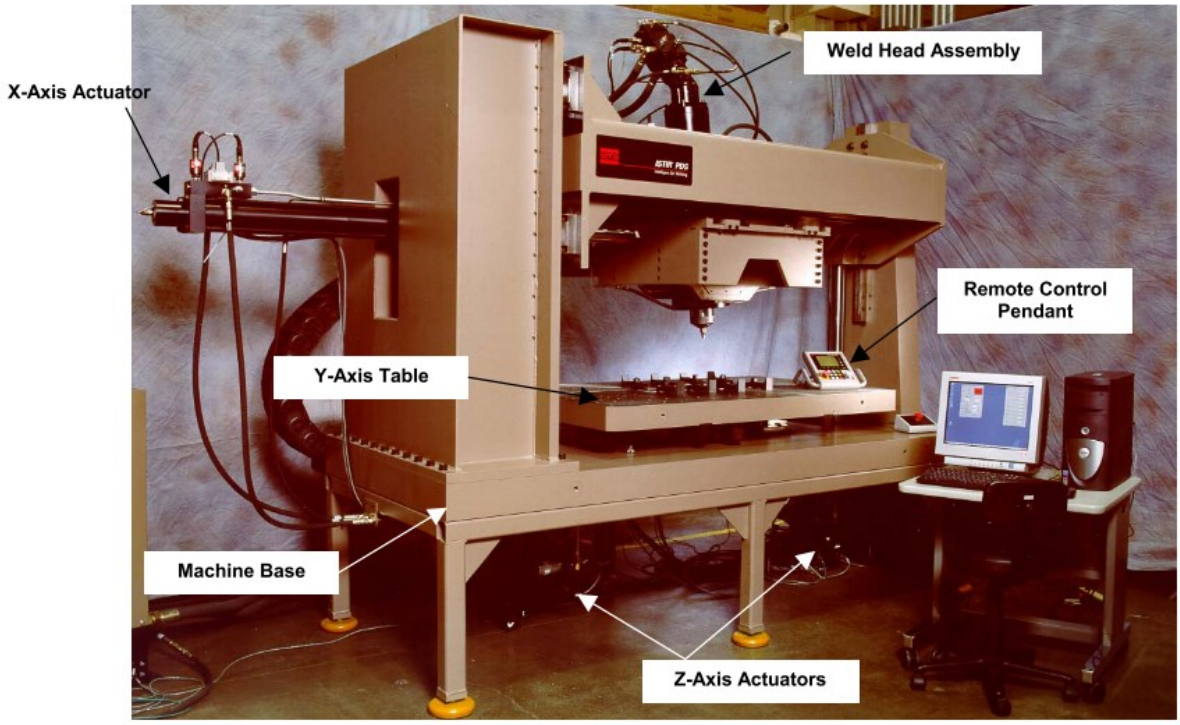

Figure 7: Friction stir processing experimental setup [65].

3.4. Characterization and Microstructural Analysis

For microstructural analysis, the cross-sectioned coated samples were cold-mounted in an epoxy resin (LECO, Mississauga, ON, Canada). The cold-mounted samples were ground using 240, 360, 400, 800, and 1200 grit silicon carbide paper (LECO, Mississauga, ON, Canada) and then polished using 3 μm and 1 μm diamond slurries (LECO, Mississauga, ON, Canada). To prevent sample charging in the scanning electron microscope (SEM), a sputter coater (ACE600, Leica Microsystems Inc., ON, Canada) was used to deposit a thin carbon coating on the samples. A SEM (Sigma, Zeiss, Cambridge, UK) was used to characterize the microstructure of the coating samples. The SEM was operated with the acceleration voltage set at 15 kV and a working distance of around 6 mm.

Images of the coating cross-section taken using SEM were used to characterize the Al_2O_3 particle content, porosity, average particle size and mean free path between the reinforcing Al_2O_3 particles. An image processing software, ImageJ (ImageJ, National Institute of Health and the Laboratory for Optical and Computational Instrumentation, Maryland, USA), was used to facilitate the measurements. The Al_2O_3 particle size and content in the coating was calculated using the thresholding feature in ImageJ, which distinguishes between the coating matrix and reinforcing particles based on the difference in contrast. This feature estimated the area of Al_2O_3 particles in the coating, which was then used to estimate the vol.% of Al_2O_3 in the coating. A similar process was conducted to evaluate the porosity in the coatings. After distinguishing the Al_2O_3 particles from the coating matrix using thresholding, the image was calibrated using the scale bar on the SEM image. The count feature of Image J was used to count the number of Al_2O_3 particles in the cross-section and evaluate the surface area of each particle to determine the particle size.

The mean free path is a measurement of the distance between the nearest Al_2O_3 particles in the coating. The mean free path is evaluated using equation 1 as follows [45]:

$$\lambda = \frac{1-v_r}{N_L} \quad [1]$$

where v_r is the volume fraction of the reinforcing Al_2O_3 particles and N_L is the number of particle intercepts per unit length. N_L was calculated by drawing a minimum of 5 lines on the SEM image of the coating cross-section and counting the number of particles intercepted by the line. The length of the line was found by using the scale bar on the SEM image for calibration. The average particle size for the Al_2O_3 particles in the coating was found using the thresholding feature in ImageJ to identify the particles and estimate the area covered by each particle. For each SEM image, a minimum of 50 particles were analyzed to achieve the average Al_2O_3 particle size measurement. For all microstructural calculations, a minimum of 4 SEM images was used with at least 5 areas of interest (n = 20).

3.5. Micro-hardness

Coating hardness was measured using a microhardness testing machine (Buehler VH1202, Lake Bluff, Illinois, USA) with a Vickers indenter in accordance with the ASTM E384-11 standard. A minimum of fifteen (n =15) measurements were taken for each coating sample at different locations in the coating cross-section to account for the variability in the coating hardness due to the non-homogeneous distribution of Al_2O_3 particles. A load of 1 kgf with dwell time a of 10 seconds was used for the measurements on all the coating samples.

3.6. Dry Abrasion Testing

Dry abrasion testing was performed on the coating samples deposited on the AA5052-H32 substrates. For dry abrasion testing, the Al-Al_2O_3 MMC coatings were deposited onto the substrates according to the sizing guidelines laid out in ASTM G65-16^{e1} [46]. Procedure E – 1000 revolutions was selected for all the coated samples. The wheel rotational speed was 200 RPM and a force of 130 N was applied to the specimen. This procedure was selected to ensure that the coating does not wear away completely to expose the underlying substrate surface. The resulting sliding distance for the selected procedure was 718 m. The abrasive used for the test was rounded quartz grain sand AFS 50/70 (U.S. Silica Co., Ottawa, IL, USA). The test wheel used was lined with chlorobutyl rubber with a hardness of approximately 60 shore A Durometer, as specified in the ASTM standard. The feed rate for the abrasive material was approximately 350 g/min. The schematic for the test assembly is illustrated in Figure 8 as per ASTM G65-16^{e1} [46]. Three samples (n = 3) were tested for each coating composition.

The loss in weight of the coating sample is measured by weighing it before and after the procedure, which allows determining the change in volume (ΔV). The wear rate (W) in mm^3/Nm can be calculated as suggested by the ASTM standard G65-16^{e1} [46] by dividing the volume loss (Δv), in mm^3 , by the applied load (P), in Newtons, and the sliding distance (s), in m, as shown in Equation (2):

$$W = \frac{\Delta V}{P * S} \quad [2]$$

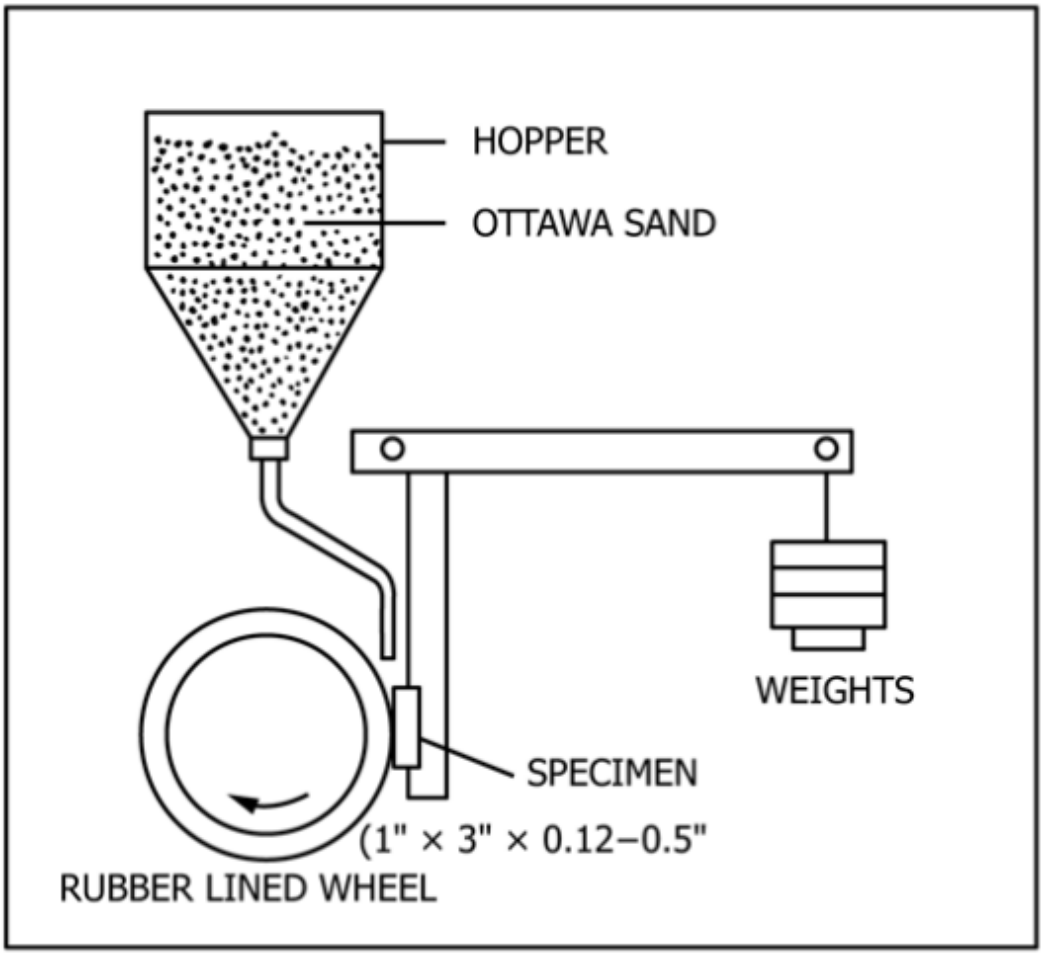

Figure 8: Schematic of the dry abrasion test assembly as per ASTM G65 [46].

3.7. High Stress Abrasion Testing

For high stress (wet) abrasion testing, the coatings were deposited onto substrates according to the specified requirements of ASTM standard B611-13 [47]. High stress abrasion testing uses a steel wheel to force the abrasive against the test surface, which creates a higher stress abrasion compared to other test methods, such as ASTM G65 [46]. The higher stress condition created by the steel wheel causes the abrasive to fracture and get crushed. A modified procedure – 25 revolutions – was selected for the high stress abrasion testing. The abrading wheel used was

made from AISI 1020 steel with a diameter of 169 mm. The rotational speed used for testing was 100 RPM. The resulting distance for linear abrasion was 13.3 m. The abrasive material used for this test was a slurry of 30-grit abrasive and distilled water. This slurry has an abrasive/water ratio of 4 grams of grit for every millilitre of water. The schematic for the experimental assembly is illustrated in Figure 9. The weight loss is found by weighing the samples before and after the test, which is used to determine the volume loss (Δv). Like the procedure for ASTM G65, the wear rate (W) is calculated using Equation 2. Three samples ($n = 3$) were tested for each coating composition

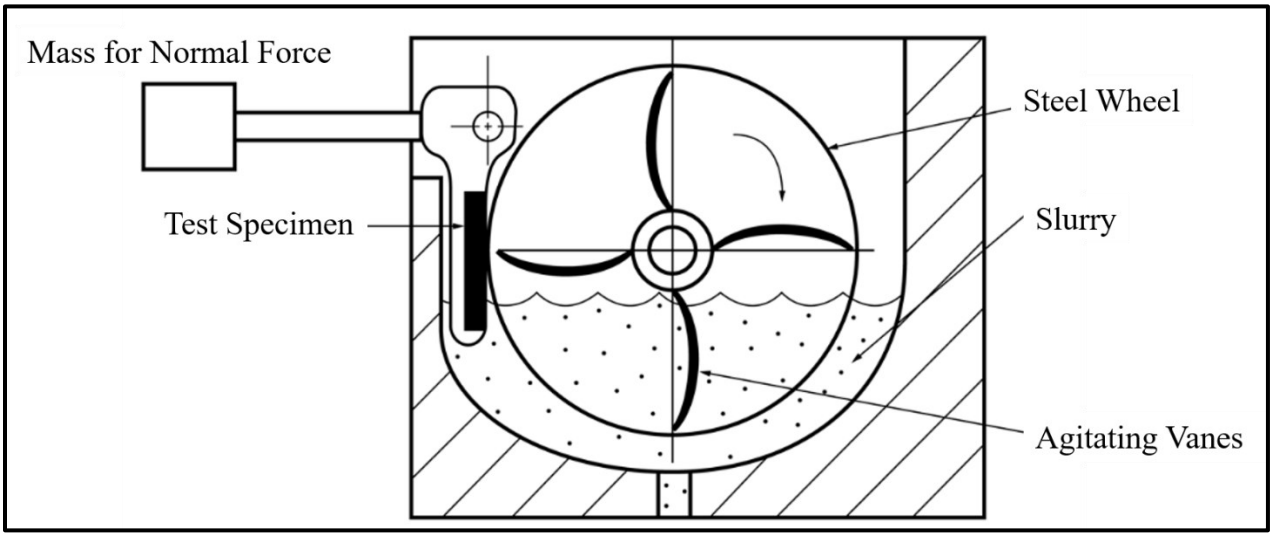

Figure 9: Schematic of test assembly for high stress abrasion testing as per ASTM B611 [47].

3.8. Strain Measurements using Digital Image Correlation

Digital Image Correlation (DIC) was used to compute the strains during the tensile tests performed in this study [16]. The strains were measured by capturing the deformation of the samples *in-situ* using a Promon U750 High Speed Camera (AOS Technologies AG, Taefernstrasse 20 CH-5405 Baden-Daettwil, Switzerland). A video of the tensile test was recorded at 100 frames/second which produced time stamped images of the test. The images were loaded into a DIC software Vic 2D 6 (Correlated Solutions, Irmo, SC, USA), and a mesh was generated for the samples, as illustrated in Figure 10. In order to achieve reliable data from DIC, a high-quality speckle pattern is required on the samples. To generate the speckle pattern on the test samples, an ultra-fine Harder and Steenbeck Infinity airbrush (Harder and Steenbeck Gmbh, Norderstedt, Germany) was used with a spray needle diameter of 0.15 m. To achieve a high contrast image, high intensity LEDs were used. An area of interest (AOI) was determined on the sample surface where the strain fields will be calculated, and a mesh was generated. The mesh size suggested by the software was 25 by 25 pixels. The mesh or subsets, as illustrated in Figure 10, were digitally tracked by the software in the subsequent time stamped images to determine the strain in the sample. The failure strain found using DIC and the failure stress from the MTS machine were matched in time to reconcile all the corresponding stresses and strains to achieve stress-strain curves.

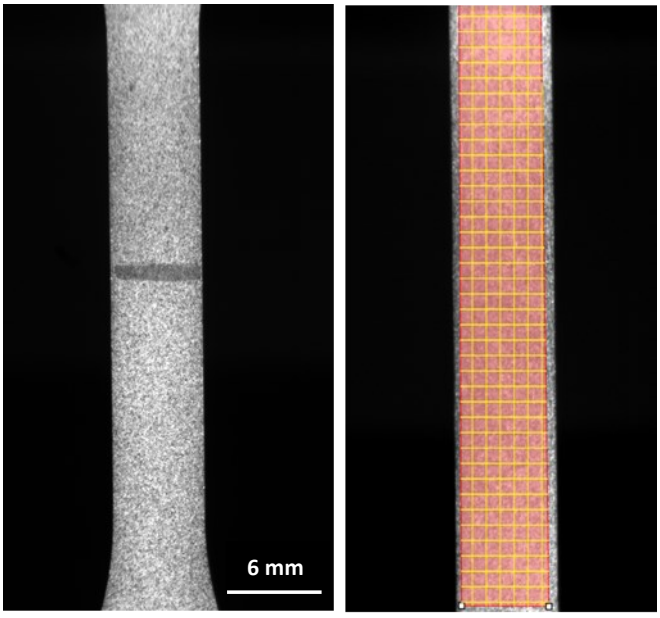

Figure 10: Image presenting (a) the surface along the reduced section of the gauge length of the tensile specimen. (b) Image showing the AOI for which the average axial strains were calculated.

3.9. Tensile Testing

Tensile testing was conducted using a universal testing system Instron 5966 (Instron, Norwood, MA, USA) located in the machine shop at the Department of Mechanical Engineering at the University of Alberta. The experimental setup is illustrated in Figure 11. The coating samples were machined to a dog bone geometry according to ASTM E8/E8M-13a [48]. The dimensions of the reduced gauge section on the samples were 25 mm in length, 6 mm in width and 1.1 mm in thickness. Since the stand-alone coating was to be tested, the coatings were extracted from the substrate material using wire-based electrical discharge machine (Agie Progress V4, Agie, 1242 Satigny, Switzerland). The samples were tested in the quasi-static regime at a loading rate of 0.0003 mm/s.

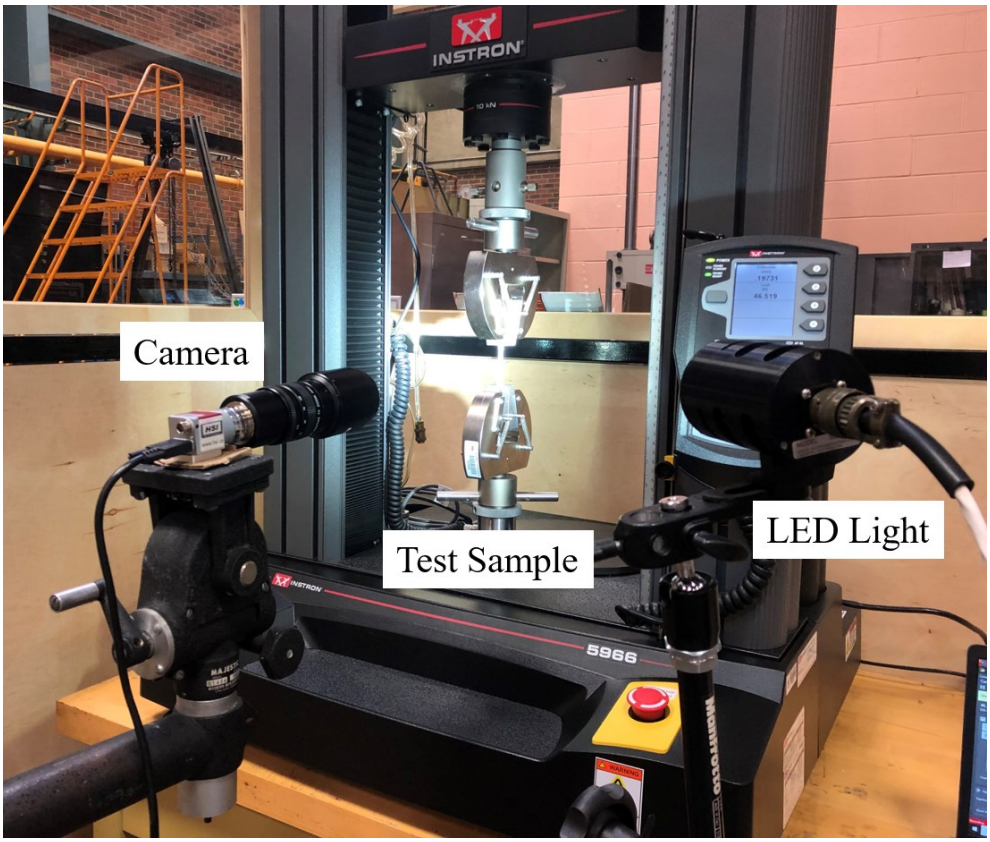

Figure 11: Tensile test assembly coupled with the DIC camera setup.

4. RESULTS AND DISCUSSION

4.1. Coating Characterization

The present study explores the improved material performance of low-pressure cold sprayed and FSPed coatings. SEM images of the coating cross-sections for both as-sprayed and post-FSPed samples were used to quantify the coatings porosity, Al_2O_3 content retained in the coating, Al_2O_3 particle size and mean free path length between the Al_2O_3 particles. Figure 12 shows the as-sprayed MMC coatings deposited using powder blends containing 10 wt.%, 50 wt.% and 75 wt.% Al_2O_3, which resulted in coatings containing 4.6 ± 0.8 wt.% (n = 3), 22.9 ± 0.6 wt.% (n = 3) and 34.6 ± 2.9 wt.% (n = 3) Al_2O_3, respectively (Figure 13). For ease of understanding and writing, the three MMC coatings will be referred to as 5 wt.%, 23 wt.% and 35 wt.% Al_2O_3 for the 4.6 ± 0.8 wt.%, 22.9 ± 0.6 wt.% and 34.6 ± 2.9 wt.% Al_2O_3 coatings, respectively. The coating cross-section images were used to determine the volume fraction of Al_2O_3, which was then converted to a weight fraction using the densities of the powders. As illustrated in Figure 13, it was observed that as the Al_2O_3 content in the powder blend increases, the Al_2O_3 content in the coating increases. Similar results were found by Hodder *et al.* [20] and Irissou *et al.* [32] where increasing the Al_2O_3 content decreased the deposition efficiency in the coating. It is hypothesized that the rebounding of ceramic particles from the substrate decreases the deposition efficiency due to the inability of Al_2O_3 particles to deform plastically during impact [28].

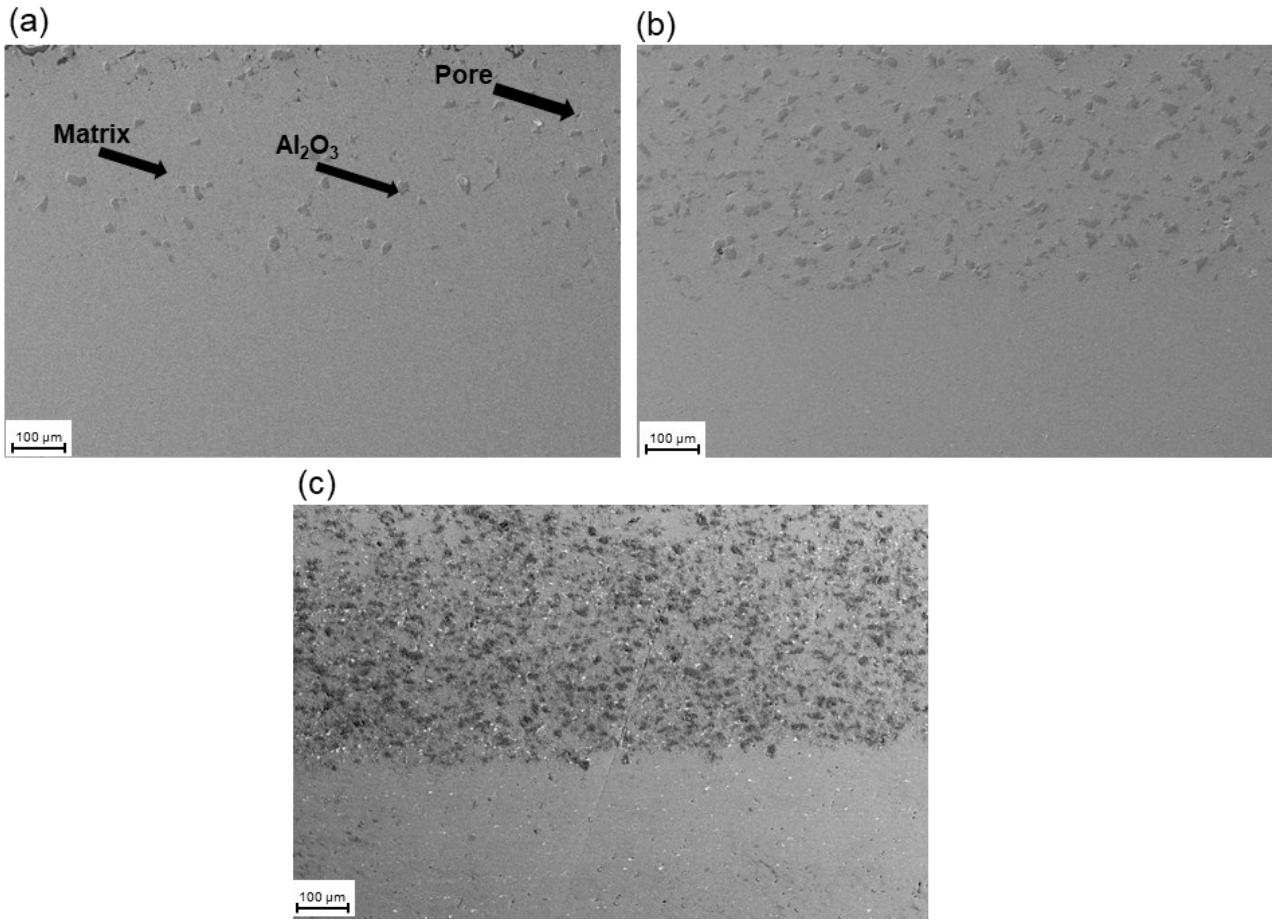

Figure 12: SEM images of the coating cross-sections of the as-sprayed coatings with (a) 5 wt.% Al_2O_3, (b) 23 wt.% Al_2O_3, (c) 35 wt.% Al_2O_3.

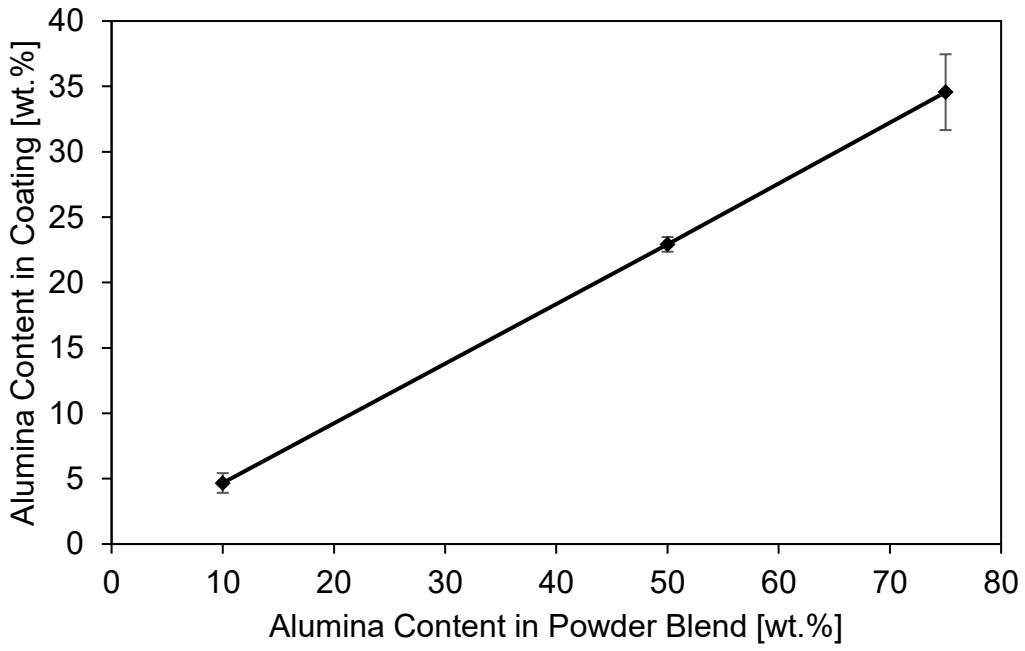

Figure 13: Graph of Al_2O_3 content in the powder blend versus that in the coating.

Figure 14 and Figure 15 show the SEM and OM images of the as-sprayed and post-FSP coatings, respectively. It was found that the Al_2O_3 particles fragmented to smaller sizes for the 23 wt.% and 35 wt.% coatings due to the impact forces during cold spray deposition. The Al_2O_3 particle fracture during deposition improves the particle distribution in the Al matrix, which is reflected by the decrease in Al_2O_3 particle size (Table 2) and mean free path measurements for the different coating samples, as illustrated in Figure 16. With increasing Al_2O_3 content in the coating, more particles fracture during deposition, as they impact previously deposited Al_2O_3 particles.

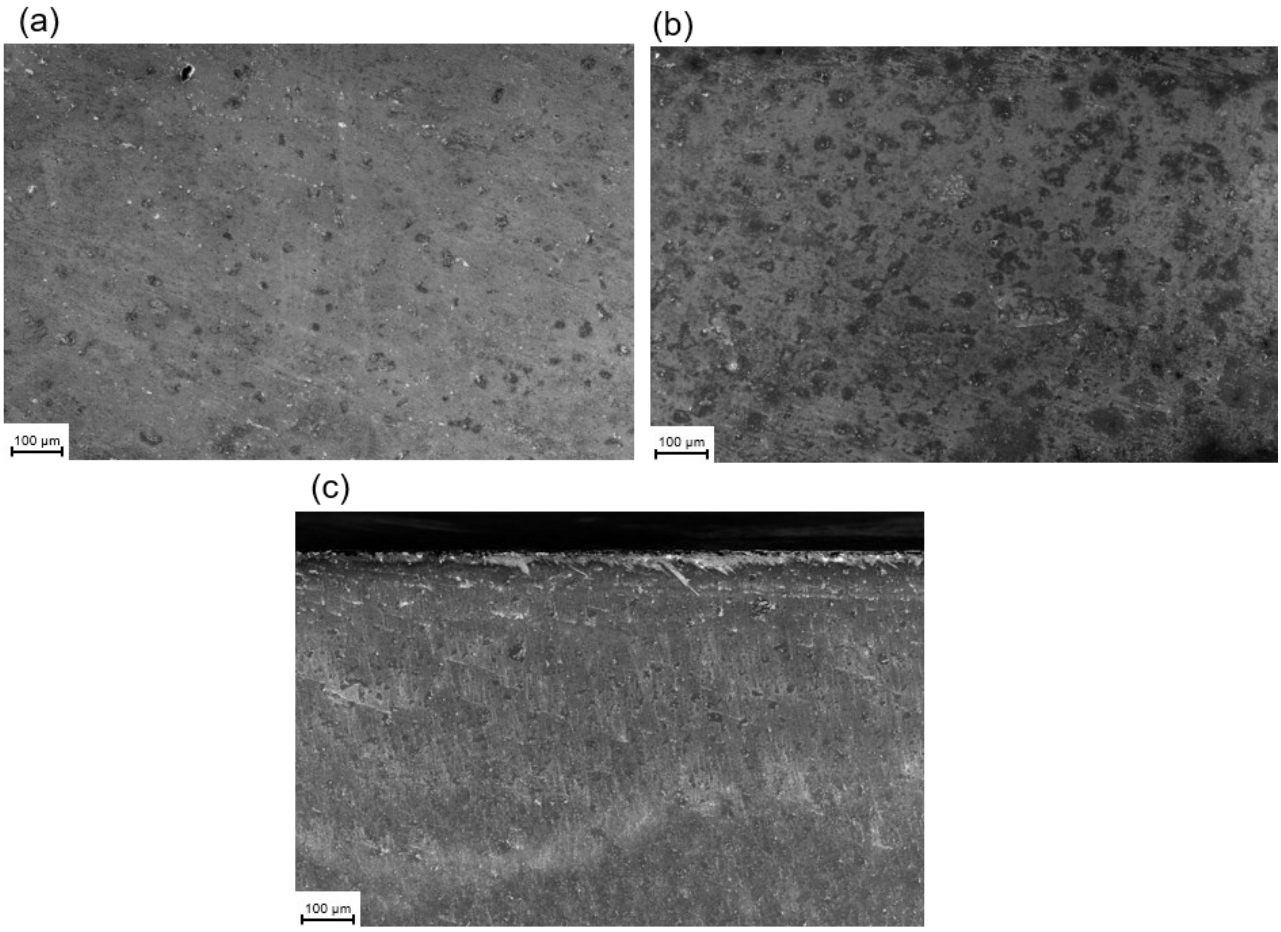

Figure 14: SEM images of the coating cross-sections of the post-FSPed coatings with (a) 5wt.% Al_2O_3, (b) 23 wt.% Al_2O_3, (c) 35 wt.% Al_2O_3.

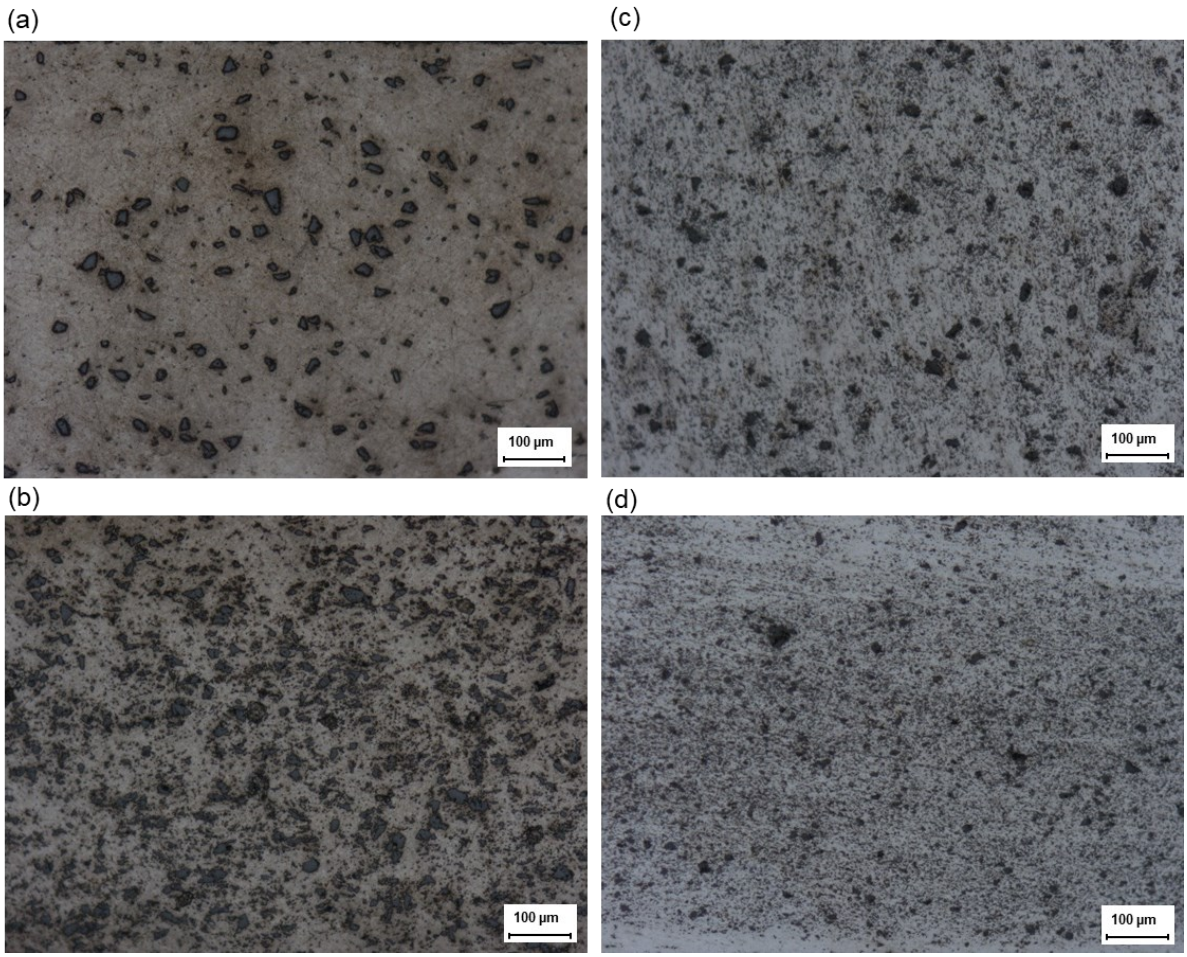

Figure 15: Images of the coating cross-sections for as-sprayed coatings (a) 5 wt.% Al_2O_3, (b) 23 wt.% Al_2O_3 and post-FSPed (c) 5 wt.% Al_2O_3, (d) 23 wt.% Al_2O_3.

Table 2: Al_2O_3 particle size in the coating for both as-sprayed and post-FSPed coatings.

Alumina Particle Size in Coating		
wt.% Al_2O_3	***As-Sprayed Size [μm^2]***	***Post-FSP Size [μm^2]***
5	144.2 ± 0.9	60.5 ± 0.1
23	97.2 ± 0.2	47.6 ± 0.1
35	34.7 ± 0.2	14.7 ± 0.0

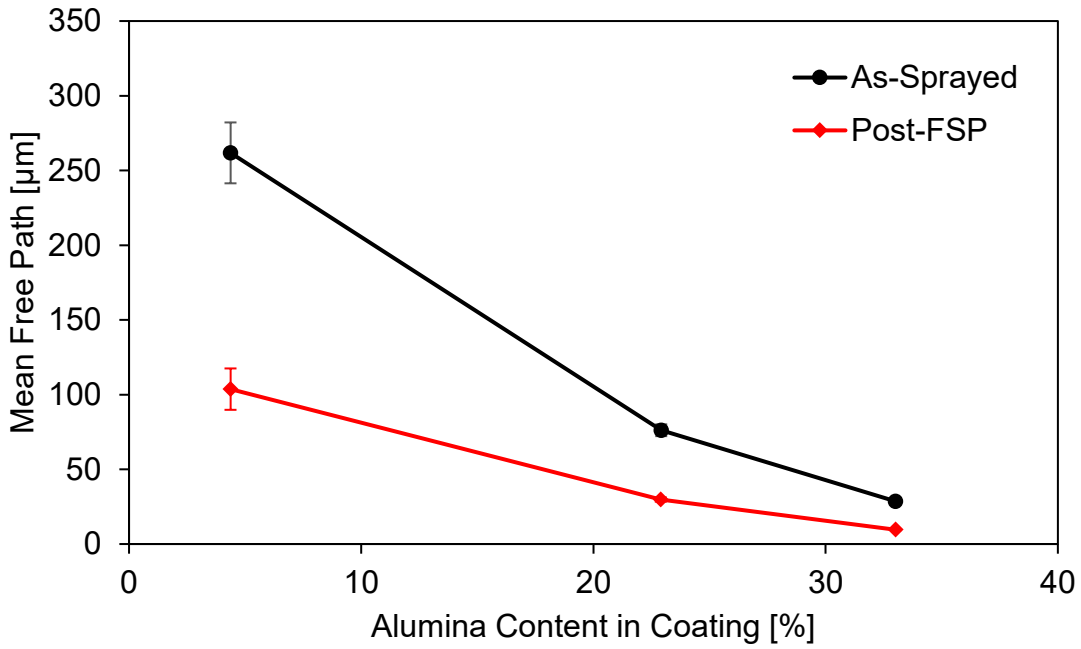

Figure 16: Mean free path between the Al_2O_3 particles versus the Al_2O_3 content in the coating.

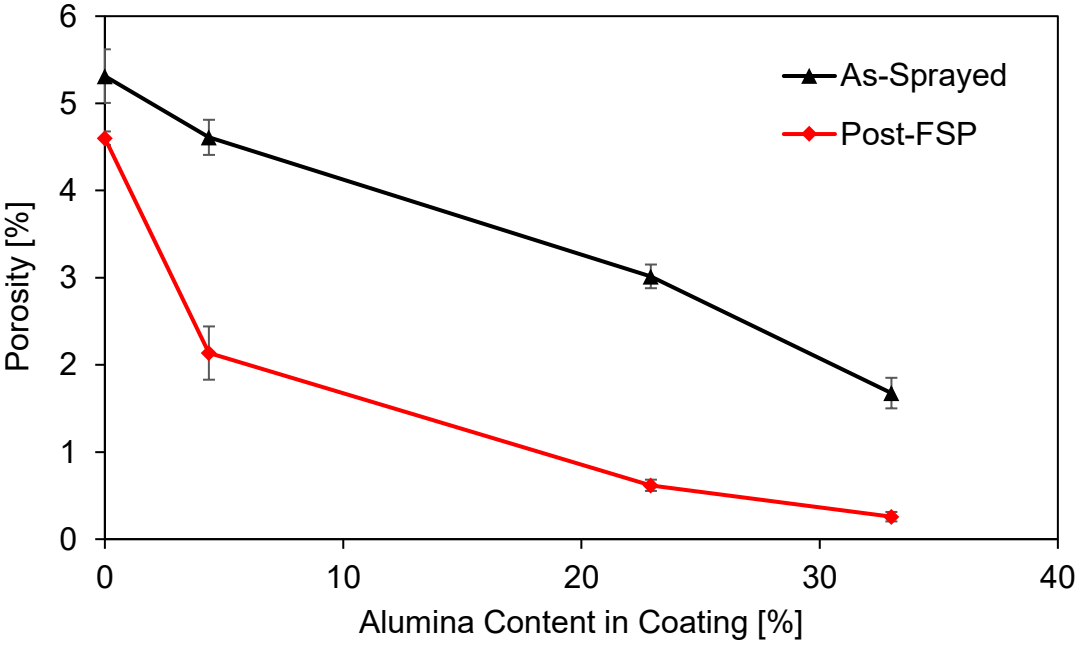

Figure 17: Coating porosity versus the Al_2O_3 content in the coating.

Following FSP, the Al_2O_3 particles appear more refined and evenly distributed through the Al matrix. The level of dispersion of Al_2O_3 increases after FSP and the particles experience further reduction in size. As shown in Figure 15, very few Al_2O_3 particles are observed that retain their initial size. The Al_2O_3 particles appear smaller and rounder post-FSP compared to their initial shape, which contains more sharp edges. This refinement and redistribution following FSP is due to the shear forces exerted by the FSP tool on the material during the stirring [6]. The stirring of the tool breaks the edges of the Al_2O_3 particles leaving smaller, rounder particles. The improved distribution of Al_2O_3 particles is reflected in the mean free path measurements, with the lowest mean free path of 10 μm belonging to the post-FSPed coating containing 35 wt.% Al_2O_3.

Figure 17 illustrates the coating porosity as a function of Al_2O_3 content in the coating for the as-sprayed and post-FSPed samples. It was found that the porosity decreased with increasing Al_2O_3 content in the coating. The highest porosity of 5.3 ± 0.3% (n = 6) corresponded to the as-sprayed pure Al coating and is attributed to the low density and irregular morphology of the Al powder particles, which can promote gas entrapment during the deposition process creating pores [20]. The reduction in porosity with increasing Al_2O_3 content can be explained by the peening effect on the coating due to repeated impact of the hard Al_2O_3 particles on the previously deposited MMC layer, which collapses pores and produces a highly dense MMC coating with reduced porosity. The porosity in the coating is reduced further after FSP as the shear force exerted during the stirring of the tool can cause the pores to collapse and promote metallurgical bonding between the particles [43]. The post-FSPed coating containing 35 wt.% Al_2O_3 exhibits the lowest porosity of 0.3 ± 0.1% (n = 6). It is believed that physical defects, such as pores, are more likely to influence the mechanical performance of materials, since pores and inclusions can be sites for void nucleation and crack propagation. Therefore, it can be hypothesized that post-FSPed coatings, with

23 wt.% Al_2O_3 and 35 wt.% Al_2O_3, will exhibit improved mechanical properties, as their porosity is below 1%.

4.2. Mechanical Performance

4.2.1. Coating hardness

Microhardness testing was conducted for all the coating samples before and after FSP (see Figure 18). A load of 1 kgf was used for the testing. Figure 18 shows that the average coating hardness increases with increasing Al_2O_3 content. For comparison, the hardness of the as-sprayed pure Al coating was found to be 41.1 ± 1.6 HV *(n = 10).* Increasing the Al_2O_3 content to 5 wt.%, increased the hardness by 20% to 49.5 ± 0.9 HV. However, a greater increase was observed for coatings containing 23 wt.% Al_2O_3 and more. The as-sprayed coating containing 35 wt.% Al_2O_3 resulted in a hardness of 72.9 ± 0.6 HV, which is a 77% increase from the as-sprayed pure Al coating. The coatings were exposed to FSP at a rotation speed of 1200 RPM. It was observed that FSP further increased the hardness of the MMC coatings. The pure Al coating experienced a 28% increase after FSP, yielding a hardness of 52.8 ± 3.1 HV. The greatest improvement in coating hardness was exhibited by the post-FSPed coating containing 35 wt.% Al_2O_3 that yielded a hardness of 83.2 ± 0.8 HV, which is 22% higher than the hardness for bulk AA5052-H32.

The dramatic increase in hardness with FSP and increasing Al_2O_3 content can be explained by the uniform distribution and refinement of Al_2O_3 particles in the post-FSPed coatings. A similar effect was observed by Hodder *et al.* [20] and Huang *et al.* [42] who concluded that FSP significantly increased MMC coating hardness by decreasing the mean free path of reinforcing particles. It has been found in previous studies that reduced porosity can also increase the hardness

of MMC coatings [20]. Using mean free path as a measure of the level of Al_2O_3 distribution in the coating, it was concluded that the coating hardness increased with decreasing mean free path between the Al_2O_3 particles (see Figure 19). It is observed in Figure 19 that there is a near linear relationship between mean free path of Al_2O_3 particles and coating hardness when the mean free path is less than 100 μm. Therefore, it can be concluded that coating hardness increases significantly when the mean free path drops below a certain threshold value, in this case 100 μm. The change in coating hardness is fairly small as the mean free path decreases from 262 μm to 100 μm, however as the mean free path decreases from 100 μm, the coating hardness increases dramatically, as reflected by the steeper slope between 0 – 100 μm in Figure 19. The greatest increase in hardness is found for the post-FSPed coating containing 35 wt.% Al_2O_3, which also exhibits the smallest mean free path of 9.6 ± 0.3 μm and the lowest porosity of 0.3 ± 0.1%. This agrees with the study performed by Kouzeli *et al.* [45], which concluded that a significant increase in hardness of MMC coatings is observed for mean free paths of less than 10 μm for the reinforcing particulate phase. In coating matrices reinforced with a higher fraction of the harder Al_2O_3 particles, the Al_2O_3 particles share the axial load applied during hardness testing, thereby reducing the load transferred to the coating matrix. Reduction in porosity also increases the hardness of the coating by creating a denser coating structure to resist the loading. Work hardening and subsequent grain refinement of the coating matrix during cold spray deposition has also shown to improve coating hardness [20, 50]. Therefore, it can be expected that work hardening would increase with Al_2O_3 content in the powder blend due to the dislocation pinning effects of these hard particles.

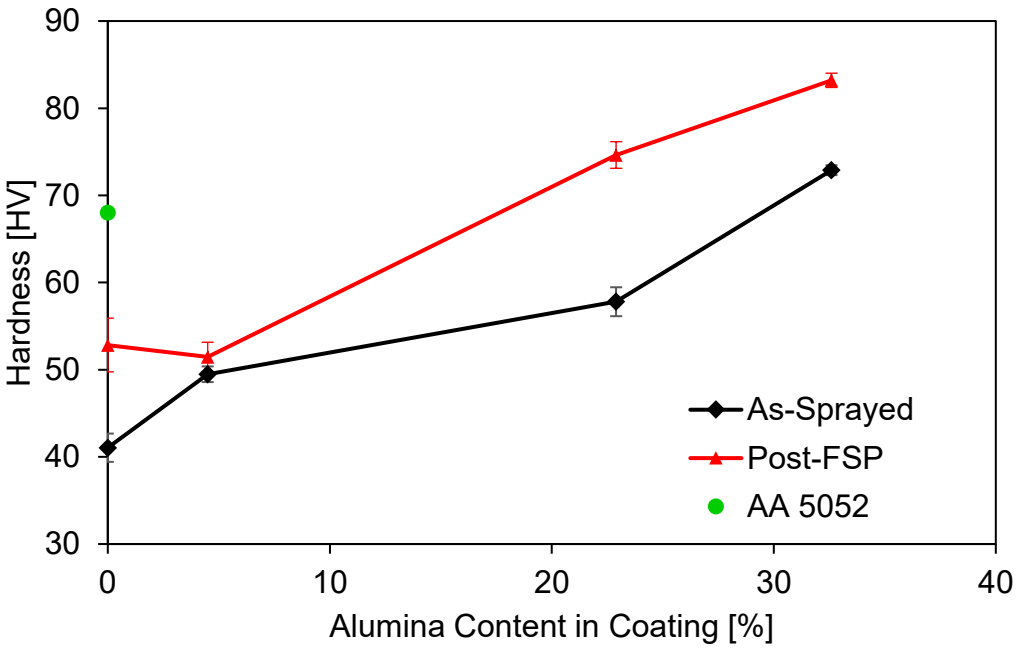

Figure 18: Relationship between coating hardness and Al_2O_3 content.

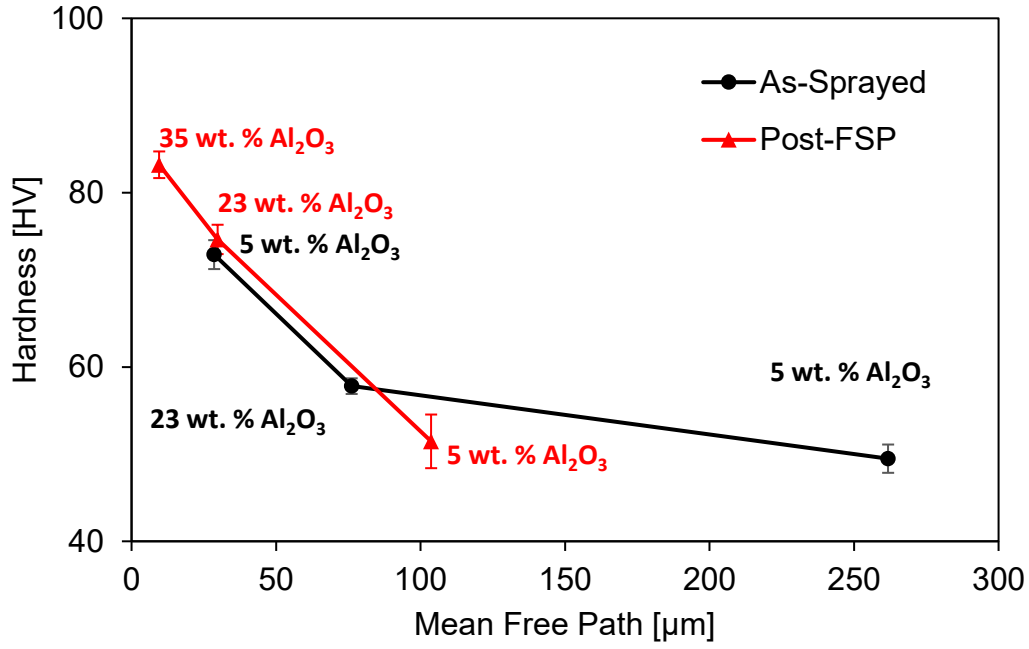

Figure 19: Relationship between the mean free path between Al_2O_3 particles and coating hardness.

4.2.2. Coating-Substrate Interface Hardness

A major drawback of FSP of cold worked metals and alloys, such as AA5052-H32, is the reduction of strength and hardness that occur in the material due to thermal softening [50]. During FSP, the stirring of the tool can raise the temperature of the stir region up to 500℃ which is higher than the annealing temperature of AA5052-H32, which is around 340℃ to 360℃ [52 - 53]. Due to the heat input of FSP being high enough to cause recrystallization in the AA5052-H32 base material [6], it is important to determine if the coating and base material interface is affected following FSP. To determine this, hardness mapping was performed for the coatings containing 5 wt.% and 35 wt.% Al_2O_3 by doing indentation measurements in different locations on the coated sample, such as the substrate, the coating-substrate interface and the coating. The results from the cross-section hardness mapping for the coating containing 5 wt.% Al_2O_3 and 35 wt.% Al_2O_3 are illustrated in Figure 20.

For the as-sprayed coating samples, the substrate and interface hardness remained around 74 HV, but slight reductions in these two regions were observed after FSP. For example, the substrate hardness for the post-FSPed coating with 5 wt.% Al_2O_3 and 35 wt.% Al_2O_3 was found to be 68.5 ± 0.3 HV (*n* = 10*)* and 61.0 ± 0.8 HV (*n* = 10*),* respectively. This minor reduction in hardness in the post-FSPed coatings can be attributed to thermal softening that is introduced into the interface and substrate during FSP. Also, since FSP was undertaken in force control mode, the material was subjected to higher normal force while processing the 35 wt.% Al_2O_3 coating relative to the 5 wt.% Al_2O_3 coating. The need for higher normal forces was due to the higher hardness of the 35 wt.% Al_2O_3 coating. It is believed that the increased normal forces during FSP of the 35 wt.% Al_2O_3 coating increased the heat input into the processing region and, in turn, led to greater thermal softening at the interface and substrate of the 35 wt.% Al_2O_3 relative to the 5 wt.% Al_2O_3

coating. As the FSP parameters for this study were tailored to ensure suitable mixing and consolidation of the coating, whilst managing overheating, another approach will need to be introduced to mitigate softening effects in the substrate that result from the higher heat input for harder deposits. Drawing inspiration from welding of dissimilar materials, under-water FSP can be considered to avoid the adverse effects of FSP on the substrate material. Researchers have explored the use of under-water FSW to lower the temperature in the periphery or heat affected regions of the central weld or stir zone, which is effective in, reducing the amount of softening, and the size of the softened zones [54–56]. Therefore, performing under-water FSP on the 35 wt.% Al_2O_3 coatings, may be a promising approach to lower the heat input from the FSP tool to substrate (so as to avoid its thermal softening), whilst imparting the (heat input) conditions necessary for adequate mixing and consolidation of the coating layer.

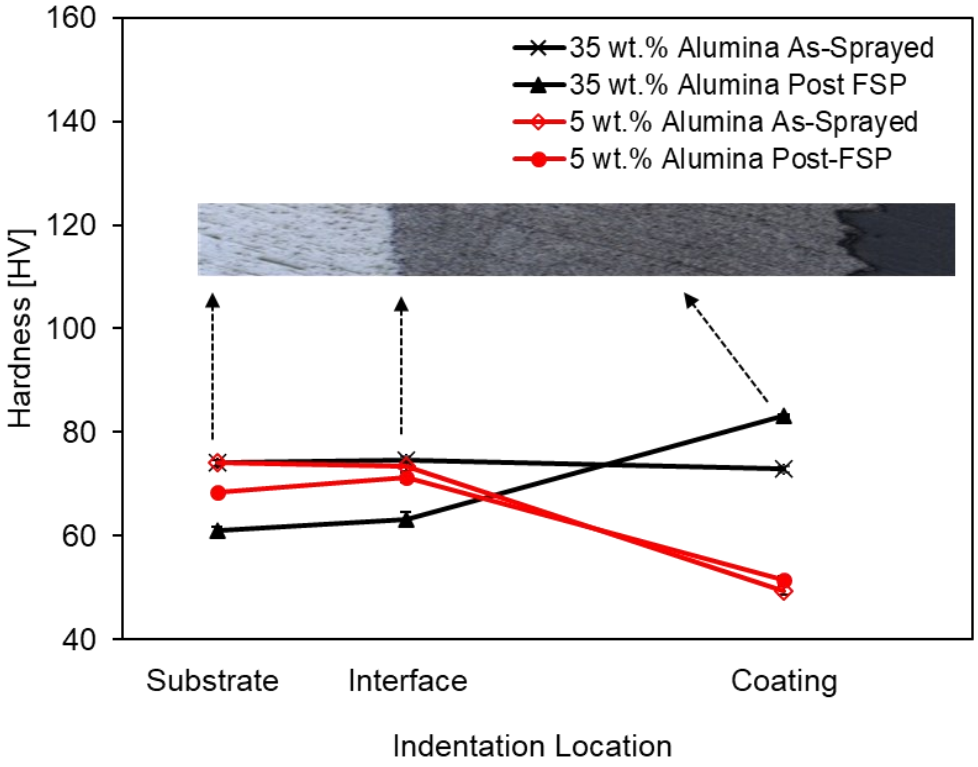

Figure 20: Hardness map tracking the hardness changes between the substrate, interface and coating for the post-FSP samples for 5 wt.% Al_2O_3 and 35 wt.% Al_2O_3 samples. The coating cross-section image is for the post-FSPed coating with 35 wt.% Al_2O_3 and is only displayed to indicate the indent location.

4.3. Mechanical performance and properties

Figure 21 illustrates the average stress-strain curves generated during tensile testing of the as-sprayed and post-FSPed coatings. The curves represent the average response of all coating samples tested. The individual sample stress-strain curves are illustrated in Appendix A. The Young's modulus was evaluated by calculating the slope of the stress-strain curves for each coating configuration. A measure of coating toughness is the energy absorbed per unit volume, which is evaluated by calculating the area under the stress-strain curve. Table 3 contains the

numerical values for the ultimate tensile strength (UTS), Young's modulus, failure strain and coating toughness. It is observed in Figure 21 (a) that increasing the Al_2O_3 content in the coating, dramatically increases the UTS of the coatings. A similar trend was found for the Young's modulus, failure strength and coating toughness. Several researchers have also found the mechanical properties to improve with increases in the reinforcing particle content for MMC coatings [25, 54, 55]. They have attributed this improvement to the refinement and improved distribution of the reinforcing particles in the matrix of the MMC coatings that comes with increasing hard particle content [58].

Figure 21 (b) illustrates the stress-strain curves for the coating samples following FSP. Analyzing the post-FSP stress-strain curve, it can be observed that contrary to the response of the as-sprayed samples, the post-FSPed samples exhibited a pronounced plastic region in their response to uniaxial tensile loading. As observed in Figure 21 (a), the as-sprayed samples exhibited limited plastic deformation before experiencing failure. Following FSP, it can be observed that the coatings undergo significant plastic deformation before experiencing failure, which is analogous to the behaviour of metals and metal alloys. Therefore, analyzing the difference between the response of the as-sprayed and post-FSPed coatings it can be concluded that FSP has an improvement effect on the tensile response of as-sprayed Al-Al_2O_3 coatings.

To analyze the improvement in the tensile strength of the as-sprayed and post-FSPed coatings, the UTS of the different coating samples was compared as illustrated in Figure 22. It can be observed that the UTS increases with increasing Al_2O_3 content for both the as-sprayed coatings and the post-FSPed coatings. The UTS increases from 49.8 ± 4.2 MPa (n = 3) for the as-sprayed pure Al coating to 157.7 ± 2.3 MPa (n = 3) for the as-sprayed MMC coating containing 35 wt.% Al_2O_3. It can also be observed that the post-FSPed coatings exhibit higher UTS values compared

to the as-sprayed coatings of the same material composition. The pure Al coating exhibited an UTS of 130.4 ± 4.0 MPa (n = 3) following FSP and the UTS increased to 171.6 ± 5.4 MPa (n = 3) for the post-FSPed coating containing 35 wt.% Al_2O_3. The largest improvement in UTS was found to be for the pure Al coatings going from 49.8 ± 4.2 MPa to 130.4 ± 4.0 MPa after FSP. This significant increase in strength can be attributed to the strengthening and consolidation effects of FSP on the as-sprayed coating. The increase in UTS with the increase in Al_2O_3 content can be attributed to a few different phenomena. Increasing the Al_2O_3 content in the coating improves the coating strength by reducing the physical defects such as pores in the coating (Figure 17: Coating porosity versus the Al2O3 content in the coating.. It was established in Section 4.1, increasing the Al_2O_3 content reduces the coating porosity, and FSP further reduces coating porosity. The strength of the coatings improves with reduced porosity as the likelihood of void nucleation and crack propagation is reduced. Another reason behind the strength improvement with increasing Al_2O_3 content is microstructural refinement [20]. Increasing the content of Al_2O_3 in the coating strengthens the coating by increasing the dislocation density in the material and creating barriers for dislocation movement. As the dislocation density increases and the oxide particles hinder dislocation movement, more force is required to deform the material, which results in improved UTS. As established in Section 4.1, the degree of distribution of Al_2O_3 particles also improves with increasing Al_2O_3 content in the coating and FSP, which is reflected in the mean free path measurements. Microstructural refinement, which causes the mean free path between Al_2O_3 particles to decrease, also improves the UTS of the coating, as it increases the dislocation density in the material [6]. However, physical defects in the material, such as pores likely dominate the materials response to external loading. This can be observed in Figure 22, where the UTS difference between the pure Al, 5 wt.% Al_2O_3 and 23 wt.% Al_2O_3 is not as dramatic as the

difference between the 23 wt.% Al_2O_3 and 35 wt.% Al_2O_3 coating samples. This is because for all the coatings with less than 23 wt.% Al_2O_3, despite the microstructural refinement of the Al_2O_3 particles, the coating response to external loading is also being affected by the porosity in the coatings which for these samples is greater than 1%. Therefore, despite the improvement in Al_2O_3 distribution in the coating material, the UTS does not increase as dramatically. Once the coating porosity reduces to below 1%, which is the case for the 35 wt.% Al_2O_3 coatings, the UTS increases dramatically as it is no longer being affected by physical defects. Another reason for improved coating strength following FSP can be the work hardening that FSP introduces into the coating matrix [6]. Since FSP introduces plastic deformation into the coating, it creates dislocations in the material and causes strain hardening in the material. This can also lead to strength improvements in the material.

In order to compare the elongation response of the coatings, the failure strain and coating toughness was analyzed for both as-sprayed and post-FSPed coatings. As illustrated in Figure 24, a remarkable increase is observed in the coating failure strain following FSP. Post-FSPed coatings exhibited failure strains that were an order of magnitude higher compared to the as-sprayed coatings. Failure strains for as-sprayed coatings ranged from 0.17% for the pure Al coating to 0.40 ± 0.02% (n = 3) for the coating containing 35 wt.% Al_2O_3. These failure strains are very small compared to the failure strains for bulk AA5052-H32, which are around 30% at room temperature. The low elongation for as-sprayed coatings can be attributed to the cold spray deposition process. Since cold spray is a solid-state deposition process, the deposition occurs due to the severe plastic deformation of powder particles during impact with the substrate. Since no melting is induced in the material, the bonding between powder particles is predominantly due to mechanical interlocking [20]. Since the mechanical bonding is the predominant bonding mechanism as

opposed to metallurgical bonding, in cold sprayed coatings, interparticle bonding is weaker compared to forged materials. Due to the weak interparticle bonding and the porosity, cold sprayed coatings often face issues of embrittlement and exhibit poor elongation [16]. It was also observed that the failure strain increased with increasing Al_2O_3 content for the as-sprayed coatings. This can be attributed to the reduced porosity that coatings with Al_2O_3 exhibit, as explored in Section 4.1. Reduced coating porosity decreases the probability of void nucleation and crack propagation, thereby delaying the fracture and enhancing the coating elongation. The failure strain for post-FSPed coatings increase by an order of magnitude compared to the as-sprayed coatings. The failure strain for post-FSP samples ranges from 2.3 ± 0.2% (n = 3) for the coating containing 35 wt.% Al_2O_3 to 11.8 ± 0.5% (n = 3) for the pure Al coating. This remarkable improvement in the coating elongation can be attributed to the consolidating and compacting effects of FSP, which lead to a denser coating. The coating porosity is reduced following FSP, which contributes to the improved elongation of the coatings following FSP. Another reason for this dramatic improvement in coating elongation following FSP can be dynamic recrystallization that occurs during FSP. During FSP, materials undergo thermoplastic deformation at high strain rates. During such processes, at high strain rates, the material experiences dynamic recovery and recrystallization, which causes grain refinement in the material [50]. Dynamic recrystallization causes grain growth in the material, which causes new grains to form. These new grains have different orientations, sizes and are less strained compared to the previous grains in the material [50]. These less strained grains are able to withstand more deformation, which improve the elongation of the material. Due to the grain refinement in the material, the number of grain boundaries increases in the material. Grain boundaries act as slip planes for dislocation movement, therefore having more grain boundaries increases the likelihood of dislocation motion which improves the elongation of the material.

During dynamic recrystallization, as grain growth occurs, the material also experiences dislocation reabsorption, which also enhances the ductility of the material [50]. Dynamic recrystallization develops in materials undergoing FSP due to the severe plastic deformation and heat input from the process and is confirmed in previous studies [6, 59]. Therefore, the dramatic improvements in the coating failure strains can be attributed to the grain refinement that occurs in the coating due dynamic recrystallization during FSP. Transmission Electron Microscopy (TEM) can be performed to visualize the grains and confirm the presence of dynamic recrystallization. Dynamic recrystallization and strengthening mechanisms during FSP are discussed in more detail in the Section 4.5. It is also observed that the failure strain decreases with increasing Al_2O_3 content for the post-FSPed coatings. This behaviour can be attributed to the effects of Al_2O_3 particles, which increase the dislocation density in the coating, hindering deformation in the material, which leads to reduced elongation and failure strain in post-FSPed coatings with high Al_2O_3 content. However, despite this reduction in elongation, the post-FSP coating containing 35 wt.% Al_2O_3 is still 6 folds greater compared to the as-sprayed coating of the same composition (Figure 24**:** Relationship between failure strain and Al2O3 content for as-sprayed and post-FSPed coatings.). This dramatic increase is attributed to the microstructural changes due to FSP. The strengthening mechanisms for FSP are explored in more detail in Section 4.5.

The amount of energy absorbed to failure per unit volume by the coating is a proxy for coating toughness [60]. Figure 23 illustrates the coating toughness measurements for all coating samples. The coating toughness was calculated by the evaluating the area under the stress-strain curve and is considered a measure of the coating strength and ductility. Similar to the elongation response, the coating toughness increases with increasing Al_2O_3 content in the coating for the as-sprayed coatings. The coating toughness for as-sprayed coatings increases from 0.047 ± 0.006

J/mm^3 for the pure Al coating to 0.364 ± 0.017 J/mm^3 (n = 3) for the coating containing 35 wt.% Al_2O_3. The increase in coating toughness with increasing Al_2O_3 content is attributed to the reduced porosity and dispersion strengthening of Al_2O_3 particles. Following FSP, the coating toughness also increased by an order of magnitude, ranging from 3.5 ± 0.6 J/mm^3 (n = 3) for the coating with 35 wt.% Al_2O_3 to 14.0 ± 0.3 J/mm^3 (n = 3) for the pure Al coating. The remarkable improvement in coating toughness is attributed to the improved ductility of the coating due to dynamic recrystallization in the material [6]. Similar results were found by Xie *et al.* [61] who performed FSP on cold sprayed nano-TiB2/AlSi10Mg composite and found the UTS and the elongation to increase significantly, due to the improved metallurgical bonding between the coating particles.

Table 3: Al_2O_3 content, Young's modulus, ultimate tensile strength, toughness and failure strain for as-sprayed and post-FSPed coatings.

	Al_2O_3 content in coating [wt.%]	***Modulus [GPa]***	***UTS [MPa]***	***Toughness [J/mm^3]***	***Failure Strain [%]***
As-Sprayed	Pure Al	32.4 ± 4.5	49.8 ± 4.2	0.047 ± 0.006	0.17
	4.5 ± 0.3	24.5	44.8	0.052	0.24
	22.9 ± 0.2	35.2 ± 1.0	93.0 ± 2.0	0.169 ± 0.019	0.31 ± 0.01
	34.6 ± 0.7	42.3 ± 1.4	157.7 ± 2.3	0.364 ± 0.017	0.40 ± 0.02
Post-FSPed	Pure Al	63.3 ± 2.4	130.4 ± 4.0	14.0 ± 0.3	11.8 ± 0.5
	4.5 ± 0.3	40.3 ± 5.1	112.6 ± 2.3	7.9 ± 0.7	7.0 ± 0.3
	22.9 ± 0.2	57.5 ± 0.8	125.1 ± 4.8	4.3 ± 1.1	3.5 ± 0.9
	34.6 ± 0.7	55.0 ± 0.7	171.6 ± 5.4	3.5 ± 0.6	2.3 ± 0.2

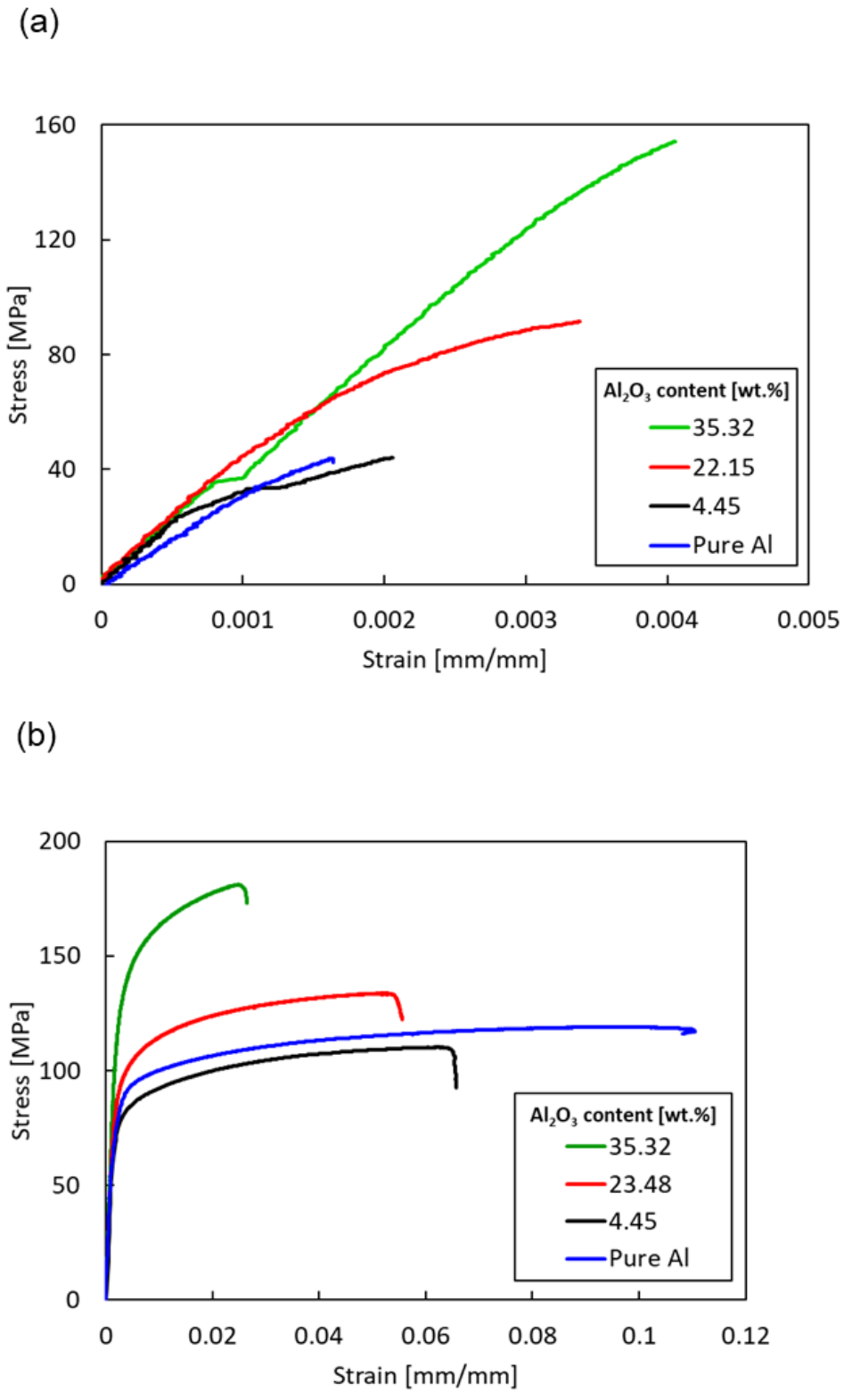

Figure 21: Average tensile stress versus tensile strain for (a) as-sprayed and (b) post-FSPed coatings. The legend indicates the wt.% Al_2O_3 for each sample.

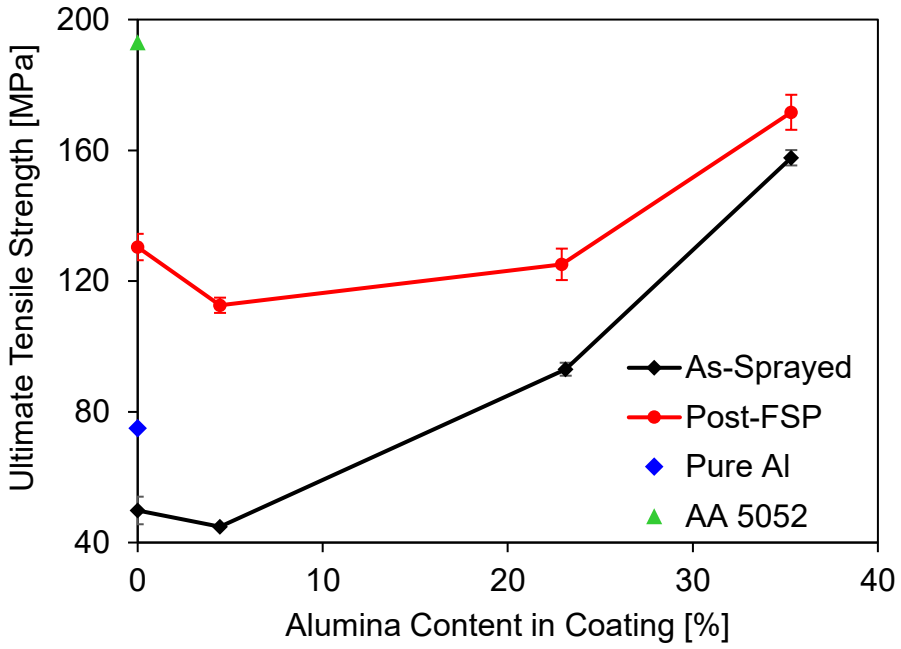

Figure 22: Relationship between ultimate tensile strength and Al_2O_3 content for as-sprayed and post-FSPed coatings.

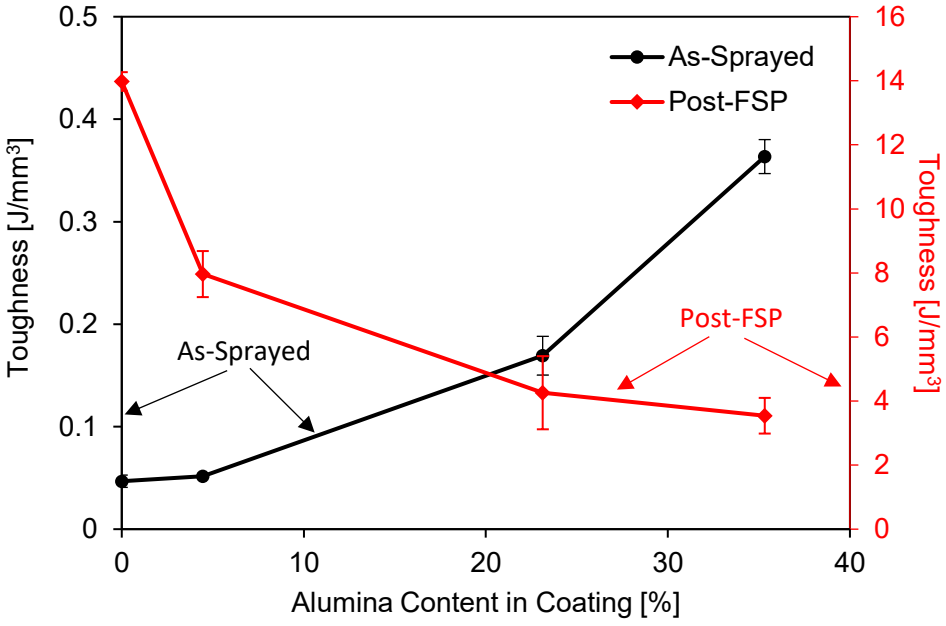

Figure 23: Relationship between coating toughness and Al_2O_3 content for as-sprayed and post-FSPed coatings.

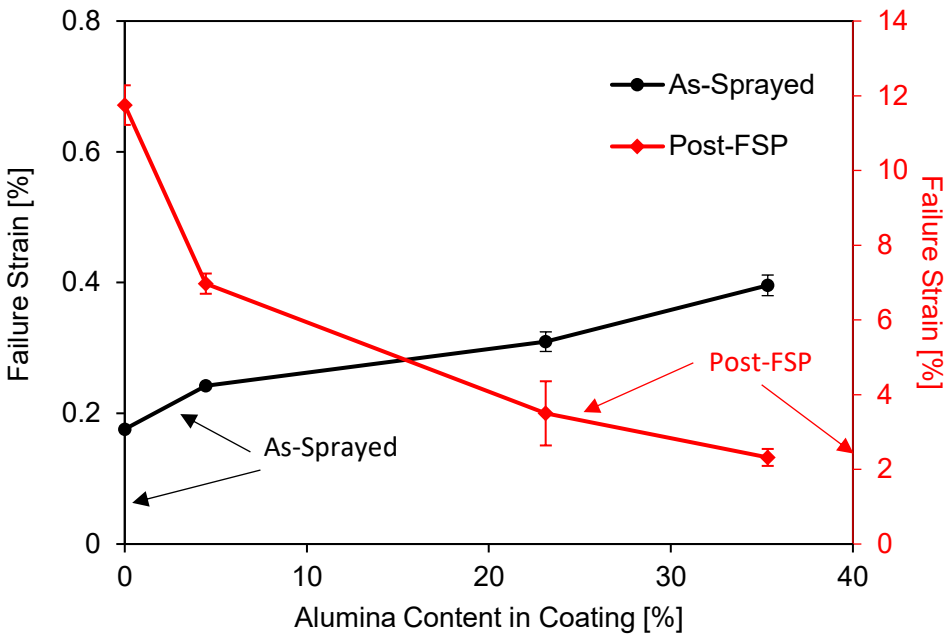

Figure 24: Relationship between failure strain and Al_2O_3 content for as-sprayed and post-FSPed coatings.

4.4.Fracture Surfaces

Images of the front view of the tensile test samples after tensile failure are shown in Figure 25. The SEM images of the fracture surface of the as-sprayed and post-FSPed coatings are illustrated in Figure 26. The microstructural differences between the as-sprayed and post-FSPed samples are evident on the fracture surfaces. It is evident that for the as-sprayed coatings, the fracture surface exhibits a very porous microstructure and the distinct particle boundaries can be observed. In Figure 26 (a-d), the individual Al and Al_2O_3 particle splats can be observed on the fracture surface, which proves the predominance of weak mechanical bonding between particles in the coating. The porous structure and weak interparticle bonding are the reasons behind the inferior elongation behaviour for the as-sprayed coatings, as porosity can cause void nucleation and crack propagation. The weak interparticle bonding leads to accelerated failure in the coating, as the failure occurs along particle interfaces rather than through them. It is also evident due to the presence of Al_2O_3 particles on the fracture surface that the bonding between Al-Al_2O_3 particles is also weak, causing the failure to occur around the Al_2O_3 particles. The absence of dimples, evident matrix particle separation and porosity are all indicative of brittle failure, which is reflected in the stress-strain curves for the as-sprayed coatings [43]. Figure 26 (e-f) illustrate the fracture surfaces for the post-FSPed coatings. The fracture surfaces for post-FSPed samples appear to have a lot of equiaxed and shear dimples on the surface. Unlike the as-sprayed coatings, the matrix particle separation and particle interfaces have disappeared for the post-FSPed coating samples indicating recrystallization of the coating matrix. The post-FSPed fracture surfaces also have reduced pores in comparison to the as-sprayed coatings. Dimple rupture is observed for the post-FSPed coatings as the fracture occurs through the particles rather than between them. Dimple rupture is indicative of stronger interparticle bonding in the matrix, a virtue of dynamic recrystallization, which leads

to a ductile fracture. The dimples indicate the resistance to tensile deformation, which can be attributed to the new, less strained grains that form during recrystallization. It was also observed that the dimples were larger and deep for the post-FSPed coating with 5 wt.% Al_2O_3 and smaller and less deep for the post-FSPed coating with 35 wt.% Al_2O_3. This can be attributed to the enhanced recrystallization due to the presence of Al_2O_3 particles. Due to the greater distribution of Al_2O_3 particles in the matrix, the recrystallization is intercepted by Al_2O_3 particles, causing more grains to form that are smaller, which lead to smaller dimples on the fracture surface. The deep dimples on the fracture surface for the post-FSPed coating with 5 wt.% Al_2O_3 are indicative of the improved elongation of the coating. Though the mode of failure is ductile due to dimple rupture for post-FSPed coatings, it can be observed in Figure 26 (h) that the failure occurs around the Al_2O_3 particle in the coating matrix, as it becomes a site for micro void growth and nucleation. However, the post-FSPed fracture surface shows successful recrystallization of the coating matrix and improved interparticle bonding, and a ductile fracture. It is also evident from Figure 25 that the post-FSPed samples for the pure Al coating and the MMC coating containing 5 wt.% Al_2O_3 experience necking in the gauge section before experiencing failure (Figure 25 (e) and (f)). This highlights further the enhanced ductility of these coatings.

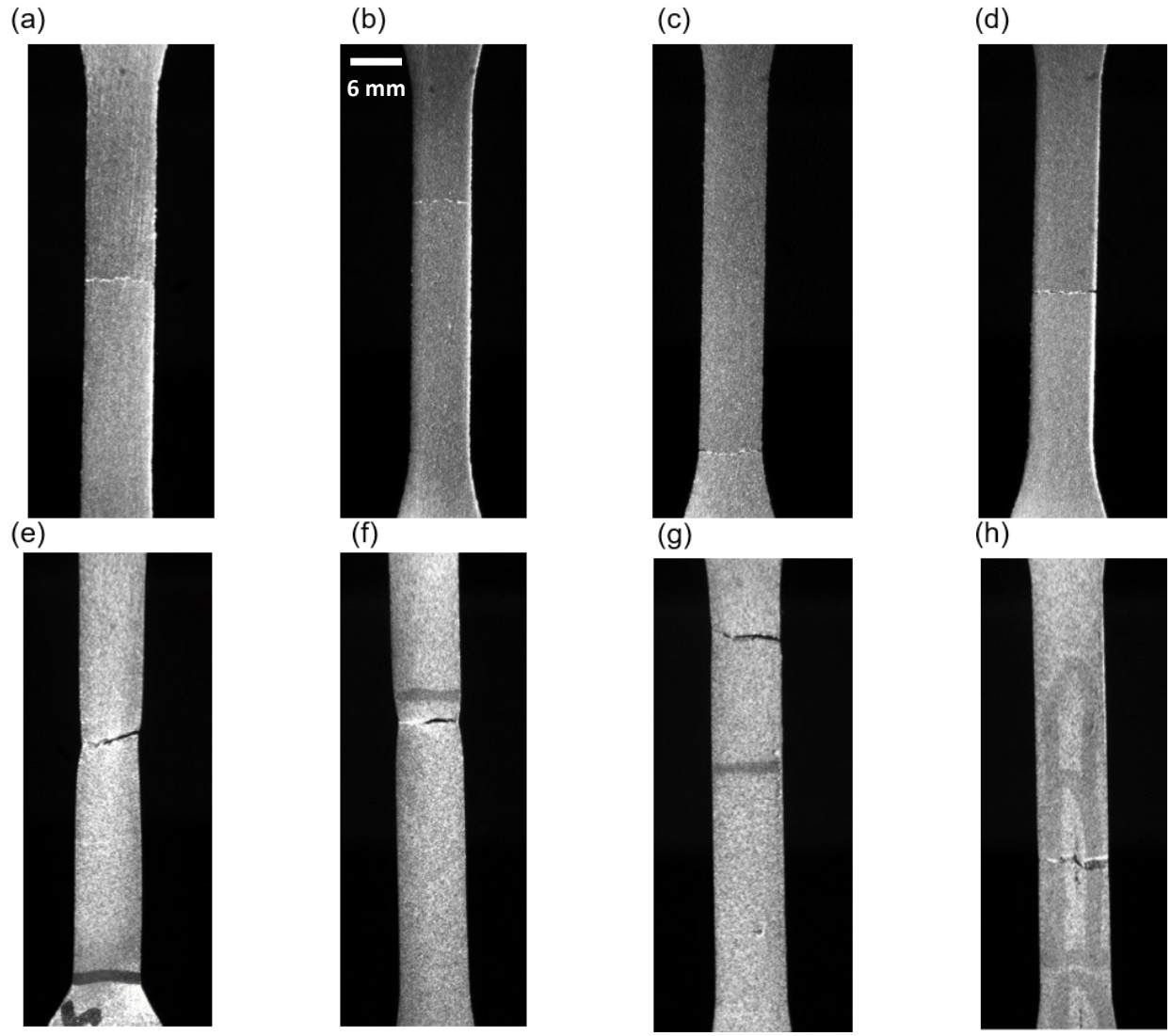

Figure 25: Images of the fracture of tensile samples for as-sprayed coatings with (a) pure Al, (b) 5 wt.% Al_2O_3, (c) 23 wt.% Al_2O_3, (d) 35 wt.% Al_2O_3 and post-FSPed coating with (e) pure Al, (f) 5 wt.% Al_2O_3, (g) 23 wt.% Al_2O_3, (h) 35 wt.% Al_2O_3.

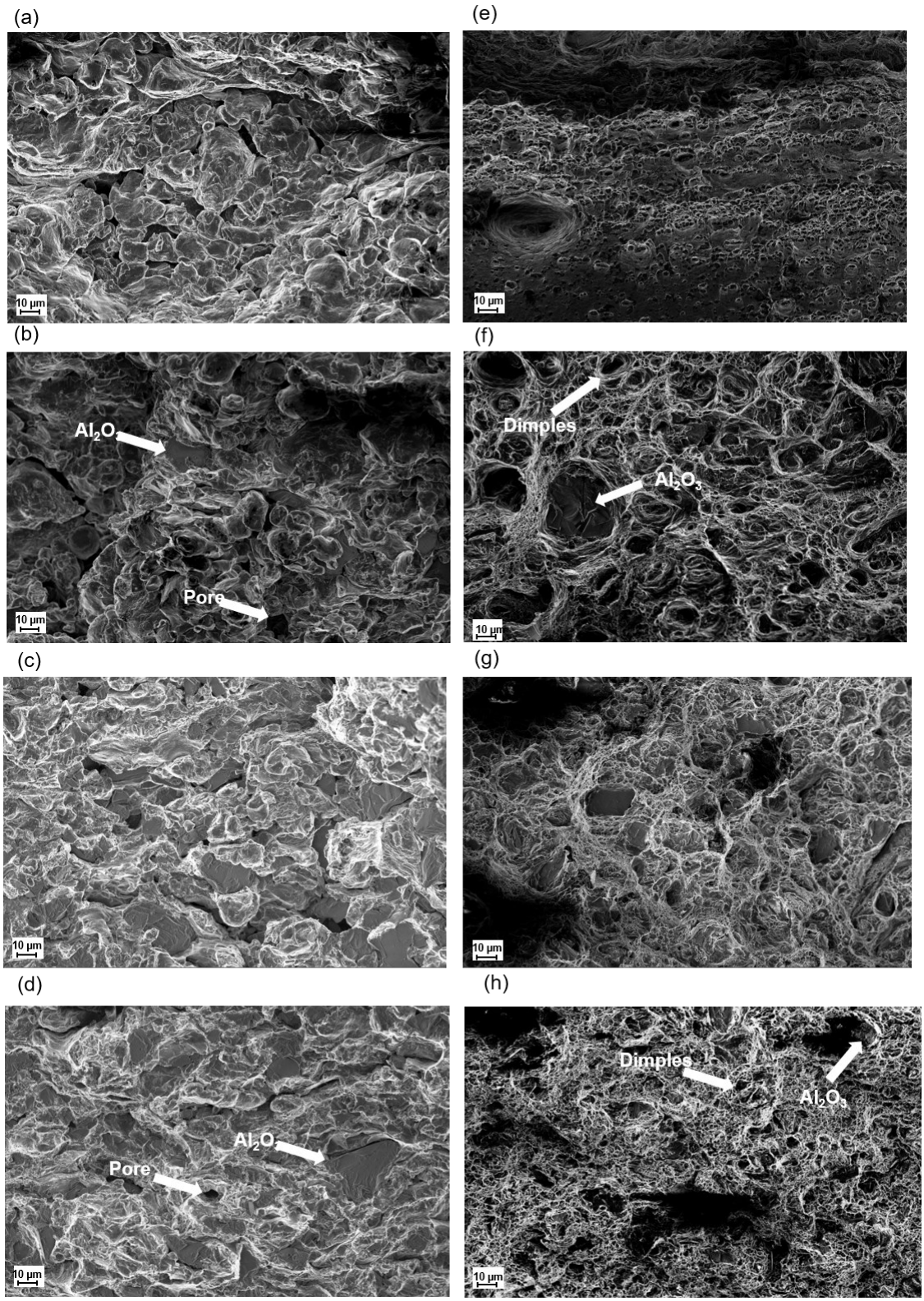

Figure 26: SEM images of the tensile fracture surfaces for as-sprayed coatings with (a) pure Al, (b) 5 wt.% Al_2O_3, (c) 23 wt.% Al_2O_3, (d) 35 wt.% Al_2O_3 and post-FSPed coating with (e) pure Al, (f) 5 wt.% Al_2O_3, (g) 23 wt.% Al_2O_3, (h) 35 wt.% Al_2O_3.

4.5. Strengthening mechanisms

The strengthening mechanisms due to the microstructure of the coatings can be analyzed, since they significantly affect the strength of the coatings when the physical defects in the coating are minimal. To better understand the strengthening mechanisms for cold sprayed and FSPed MMC coatings, a combined linear law is suggested. The flow stress for the MMC coatings can be described as follows:

$$\sigma_{FS} = \sigma_{YS} + \sigma_{\rho} + \sigma_{HP} + \sigma_{OR} \quad [2]$$

where σ_{FS} refers to the flow stress for the MMC coatings. Since these are MMC coatings that have been fabricated using cold spraying and FSP, there are various contributors to the overall strength of the coatings including the yield strength σ_{YS} contribution from the Al matrix, stress contribution due to the dislocation density σ_{ρ}, the stress contribution due to the matrix grain size according to the Hall-Petch criteria σ_{HP} and the contribution due to oxide dispersion strengthening or Orowan strengthening, σ_{OR}. For the case of as-sprayed Al-Al_2O_3 MMC coatings, the contribution from change in grain size is considered negligible since no significant grain refinement will likely occur in the matrix during deposition; therefore, σ_{HP} can be ignored for the as-sprayed coatings. The main contribution to the tensile strength of as-sprayed coating is due to Orowan strengthening. According to the Orowan formula:

$$\sigma_{OR} \propto \frac{\sqrt{v_r}}{\varphi}. \quad [3]$$

The stress contribution from Orowan strengthening is directly proportional to the volume fraction of the Al_2O_3 particles (v_r) and the average size of the Al_2O_3 particles in the coating (φ). Therefore, as the Al_2O_3 content in the coating increases, the tensile strength increases, as more oxide particles

create barriers for dislocation movement, thereby resisting plastic deformation. As established previously, the Al_2O_3 particle size decreases with increasing Al_2O_3 content in the coating. The breakup of particles lowers their size, which further enhances the dispersion strengthening effects in the coating. The oxide particles act as dislocation pinning sites, creating additional barriers for dislocation movement, thereby requiring increased force to cause plastic deformation. A similar strengthening phenomenon, synergistic strengthening, was observed by Shao *et al.* [62] who found that increasing ceramic content in an as-sprayed MMC coating improved the yield strength of the coatings due to the improved ceramic content distribution and in-situ strain hardening of the matrix during cold spray deposition. The post-FSPed coatings exhibit increased UTS due to the Al_2O_3 particle sizes being lower than for the as-sprayed coatings with the same Al_2O_3 content. This increases the contribution from Orowan strengthening and produces coatings with higher UTS.

The improved tensile properties of the post-FSPed coatings can also be explained by the additional strengthening effects due to the grain refinement that occurs in the material during FSP. During FSP, the material experiences thermoplastic deformation at high strain rates. This causes the material to undergo dynamic recrystallization and consequently grain refinement. The grain refinement that occurs in the coating matrix decreases the average grain size in the matrix. According to the Hall-Petch criteria:

$$\sigma_{HP} \propto \frac{1}{d} \qquad [4]$$

where *d* is the distance between adjacent dislocations in the material. It was found following FSP, the fracture surfaces presented an abundance of dimples, which was absent for the as-sprayed samples. The abundance of dimples and fracture through the particles proves the occurrence of recrystallization and consequent reduction in grain size in the coating matrix. As the grain size

decreases due to refinement after FSP, as indicated by the dimpled fracture surfaces, there are more grain boundaries closer together, which decreases the value for d thereby increasing the overall strength of the material. Therefore, it is widely understood that a reduction in grain size leads to an increase in material strength. Though the contribution from grain refinement is not as large as the contribution from Orowan strengthening, it contributes to the overall strength of the coatings yielding higher UTS values for post-FSPed coatings. Since it is expected that the grain refinement following FSP is significantly larger than any grain refinement in the as-sprayed coatings, this contribution can be ignored for the as-sprayed coatings [6].

The remarkable improvement in the elongation and toughness of the post-FSP coatings compared to the as-sprayed coatings can be attributed to the strain hardening and dynamic recrystallization that occurs in the material during FSP. During FSP, the material undergoes thermoplastic deformation, as the temperature in the stir zone can be significantly elevated. To understand the effects of this thermoplastic deformation, a physical constitutive model is considered, which uses the dislocation density, ρ, as an internal variable of the microstructural evolution in the material. According to the dislocation density theory [63]:

$$\sigma_\rho \propto \sqrt{\rho}\,. \qquad [5]$$

The Kocks and Mecking (K-M) model is used to trace the microstructural evolution in the material. During a thermoplastic deformation process, the microstructural evolution depends on the competition between strain hardening and dynamic recrystallization [50]. During strain hardening, materials are strengthened by dislocation multiplication that occurs in the materials increasing the dislocation density. Increased dislocation density increases resistance to plastic deformation thereby improving the tensile strength of the material. Due to the high temperature and strain rates

involved in FSP, after a certain threshold strain, the material also undergoes dynamic recovery and recrystallization [6], [26]. During dynamic recrystallization, the material experiences grain growth and refinement, which leads to dislocation annihilation or reabsorption. This lowers the dislocation density in the material. The K-M model suggests that the dislocation evolution in the material during a thermoplastic deformation process occurs according to the equation:

$$\frac{d\rho}{d\varepsilon} = k_1\sqrt{\rho} - k_2\rho \qquad [6]$$

where k_1 is the strain hardening coefficient and k_2 is the dynamic recrystallization coefficient. The interactive effects of strain hardening and dynamic recrystallization, as experienced in FSP, are likely responsible for the improved tensile strength and elongation of the post-FSPed coatings. The remarkable enhancement in the elongation of the post-FSPed coatings can be attributed to the grain growth and refinement that takes place during dynamic recrystallization. During dynamic recrystallization, grain growth occurs creating new grains that are less strained. The new grains have different orientations and sizes and create much finer grain boundaries. These new, less strained grains can withstand greater elongation before experiencing failure. The refined grain structure introduces finer grain boundaries, which significantly enhance the ductility of the material by increasing the number of slip planes for dislocation movement along the grain boundaries allowing for sustained deformation. Therefore, during FSP, the effects of dynamic recrystallization dominate the effects of strain hardening at high strain rates, as according to the K-M model the dislocation density begins to decrease in the material allowing for greater elongation and consequently greater toughness for the coatings.

4.6. Abrasion performance

Dry abrasion and high stress (wet) abrasion tests were performed for the as-sprayed and post-FSPed coating samples as per ASTM G65 and ASTM B611, respectively. The wear rate of the as-sprayed and post-FSPed coating samples for dry abrasion testing is illustrated in Figure 27. Following the trend of the coating hardness, the wear rate was found to decrease with increasing Al_2O_3 content in the coating for both as-sprayed and post-FSPed coatings. The wear rates were between $85.8 \times 10^{-5} \pm 2.8 \times 10^{-5}$ mm^3/N-m (*n* = 3*)* and $97.3 \times 10^{-5} \pm 0.9 \times 10^{-5}$mm^3/N-m (*n* = 3*)* for the as-sprayed coating samples. Following FSP, the wear rate for the coatings decreased further yielding the lowest wear rate for the post-FSPed 35 wt.% Al_2O_3 of $81.6 \times 10^{-5} \pm 1.4 \times 10^{-5}$ mm^3/N-m (*n* = 3*)*. Though the wear rates for the as-sprayed and post FSPed coating containing 35 wt.% Al_2O_3 are similar, it would require more statistical rigour and additional test repetitions to determine if the values are different statistically. In particular, as FSP involves high temperatures during the process, it can introduce thermal softening into the coating, which can negatively affect the abrasion resistance of the material. However, the comparable if not improved wear resistance of the post-FSPed coatings indicates that the effect of thermal softening on the wear resistance was lower than the improvements in the wear resistance due to improved consolidation, ceramic particle distribution and interparticle bonding following FSP. The enhanced wear performance of the post-FSPed coatings demonstrates the advantages of FSP for erosion performance and can be attributed to the improved particle distribution and consolidation of the coating which improves the interparticle bonding in the coating also contributes to the improved wear resistance. The reduced mean free path between Al_2O_3 particles after FSP reflects the improved dispersion and refinement of the Al_2O_3 particles in the coating matrix, which increases the hardness of the coating through load sharing. Due to this improved hardness of the coating, the

depth of the erosion due to the abrasive particles is limited, which consequently improves the wear performance of the coating [26]. A similar correlation between hardness and wear performance has been explored for other thermal spray coatings as well [26]. The pure Al coating experiences a drop of 13% in the wear rate after FSP. This can be explained by the work hardening that occurs in the coating matrix during FSP. Uniform deformation in a material leads to an increase in the statistically stored dislocations due to strain localization in the matrix, which contribute to the strain hardening of the material [20]. A strain hardened microstructure is more resistant to deformation and exhibits improved hardness and thereby exhibits improved wear resistance. It was observed that the wear rate for the post-FSPed coating with 5 wt.% Al_2O_3 was higher than the post-FSPed pure Al coating. This can be attributed to the agglomeration and uneven distribution of Al_2O_3 particles that is experienced in the 5 wt.% Al_2O_3 coating as reflected by the high mean free path values. The agglomerated Al_2O_3 particles may increase the wear rate as removal of these agglomerates would lead to a larger loss in volume of the coating as compared to the volume loss experienced by the smaller, more evenly distributed Al_2O_3 particles. Considering the wear behaviour for the various coatings, it can be suggested that the abrasive particles remove the soft, ductile Al matrix first that surrounds the Al_2O_3 particles. Continued exposure to the abrasive particles then causes the hard Al_2O_3 particles to be pulled from the coating surface. Similar wear behaviour was found by Peat *et al.* [21] with cold sprayed WC-Co coatings.

The results from high stress abrasion testing are illustrated in Figure 28. It was found that the wear rate for the coating samples was 3 orders of magnitude higher for the high stress (wet) abrasion testing compared to the results from dry abrasion testing. The wear rate for high stress abrasion testing was found to be between $15.1 \times 10^{-3} \pm 0.8 \times 10^{-3}$ mm^3/Nm ($n = 3$) and $23.1 \times 10^{-3} \pm 1.4 \times 10^{-3}$ mm^3/Nm ($n = 3$) for the as-sprayed coatings. For both as-sprayed and

post-FSPed coatings, the wear rate decreased significantly from the pure Al and 5 wt.% Al_2O_3 coating going from $22.9 \times 10^{-3} \pm 0.7 \times 10^{-3}$ mm^3/Nm ($n = 3$) to $15.4 \times 10^{-3} \pm 0.9 \times 10^{-3}$ mm^3/Nm ($n = 3$), respectively; however, little variation with increasing Al_2O_3 content was observed after that. The wear rates for the 23 wt.% and 35 wt.% coatings were similar, however slightly lower post-FSPed than their as-sprayed forms. As implied by the name of the test, high stress abrasion testing involves using a steel wheel and an abrasive slurry to introduce erosion on the coating surface, which produces a higher normal stress between the wheel and coating surface compared to the dry abrasion test setup. This normal stress is high enough to cause the abrasive particles to fracture against the coating surface, reducing them in size, which accelerates the wear [47]. It appears that the softer, ductile, unreinforced matrix erodes faster than the Al_2O_3 reinforced matrix due to the increased stress during abrasion. The wear rate decreased for the Al-Al_2O_3 MMC coatings compared to the pure Al coating; however, the wear rates were still significantly higher compared to the wear rates for dry abrasion testing. The grit used for high stress abrasion testing has a size of around 600 μm according the ASTM B611 [47]. However, since the grit particles break and fracture between the steel wheel and coating surface, they further reduce in size. The reduced size of the grit particles accelerates wear as the grit particles become smaller than the mean free path between Al_2O_3 particles in the coating. This allows the grit particles to erode more of the coating matrix without interacting with the Al_2O_3 particles. Therefore, the wear rate is higher for as-sprayed Al-Al_2O_3 MMC coatings compared to the post-FSPed coatings, as the mean free path is larger for the as-sprayed coatings. Since the wear rates for the as-sprayed and post-FSPed coating containing 35 wt.% Al_2O_3 are comparable to each other considering the standard deviation, further test repetitions of the same samples would be required to determine conclusively if the values are statistically significant. Similar to the dry abrasion test results, it can be concluded based

on the results that FSP did not introduce any thermal softening effects in the coating and did not negatively affect the coating abrasion performance.

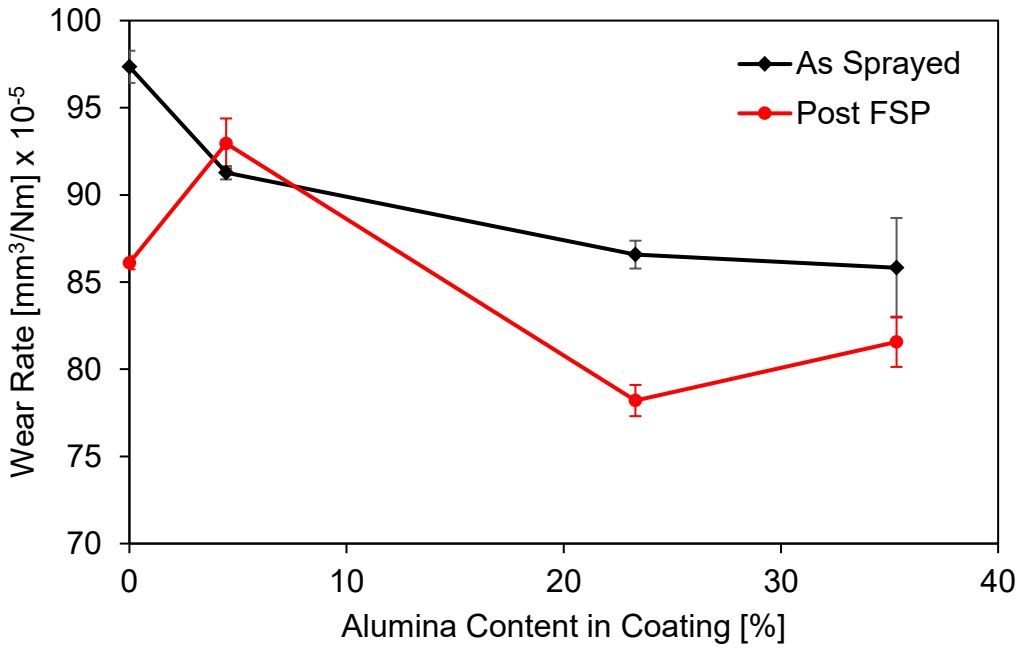

Figure 27: Dry abrasion wear rate versus Al_2O_3 content for as-sprayed and post-FSP coatings.

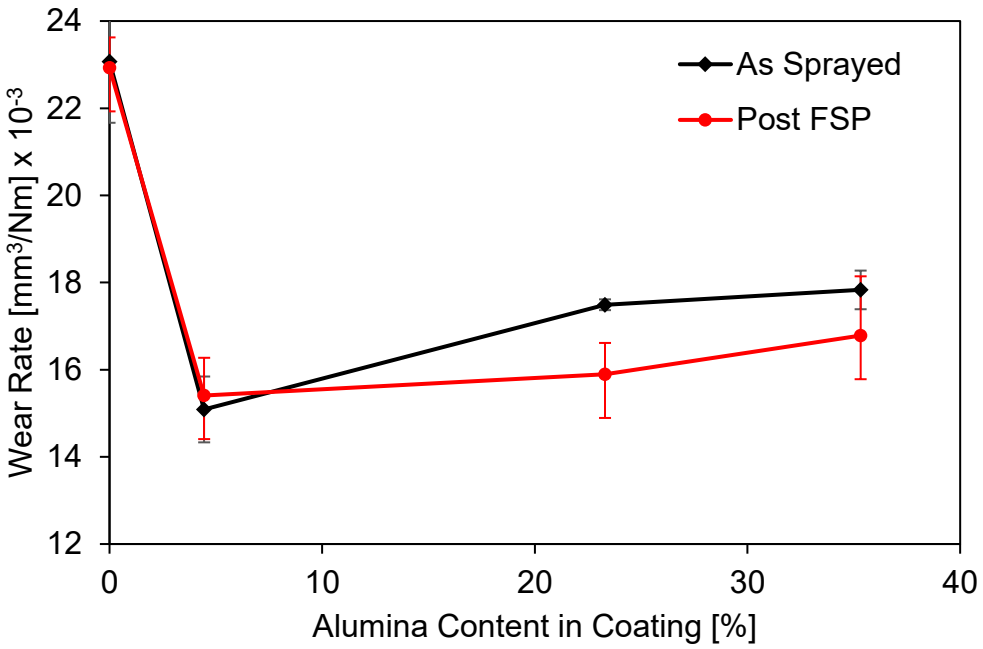

Figure 28: High stress abrasion wear rate versus Al_2O_3 content for as-sprayed and post-FSP coatings.

5. CONCLUSION

This study concluded that cold spray-FSP repair methodology successfully enhanced the mechanical properties of Al-Al_2O_3 MMC coatings. The focus of this study was to propose a novel methodology of repairing high strength cold worked aluminum alloys, specifically AA5052-H32, using MMC coatings fabricated using two advanced solid-state processing technologies: cold spraying and FSP. Recognizing the advantages and disadvantages of both cold spraying and FSP, it was decided that both processes be combined to create coatings with improved mechanical properties that can be used to perform surface modification and repairs for the unrepairable AA5052-H32. Harnessing the potential of cold sprayed MMC coatings, it was decided to use Al-Al_2O_3 MMC coatings to fabricate relative thick coatings (2.5 mm) that would emulate overlay thicknesses of interest. To analyze the effect of the reinforcing Al_2O_3 phase, the coatings were fabricated with various Al-Al_2O_3 powder blends, including a pure Al powder blend and 3 powder blends that yielded coatings containing 5 wt.%, 23 wt.% and 35 wt.% Al_2O_3, respectively. The coating samples were then FSPed using a cylindrical tool with the shoulder penetrating the coating surface. The FSP parameters were decided with the goal of keeping the coating as cold as possible by minimizing the frictional heat input into the coating. Coating characterization was performed to compare the microstructure of the as-sprayed and post-FSPed samples using SEM, OM, EDX and image analysis. Vickers microhardness indentation and uniaxial tensile tests were performed on the stand-alone coatings to characterize their mechanical performance. Dry and high stress abrasion testing was also performed to determine the wear performance of the various coatings. The strengthening mechanisms for cold sprayed MMC coatings and FSP were explored to explain the changes between the mechanical and wear performance between the as-sprayed and post-FSPed coatings.

It was determined that increasing the Al_2O_3 content in the coating improved the coating hardness for the as-sprayed coatings, and FSP further improved the coating hardness. The highest hardness was achieved for the post-FSPed coating with the highest amount of Al_2O_3 content examined in this study (35 wt.%), which exceeded the hardness of the AA5052-H32 substrate material. The increase in the hardness with increasing Al_2O_3 content was related to the improved distribution of Al_2O_3 particles throughout the coating matrix. It was also found that FSP caused the Al_2O_3 particles to break up into smaller particles and get redistributed through the coating matrix, creating greater areas of reinforced matrix. The improvement in hardness was related to the level of Al_2O_3 dispersion in the matrix as represented by the mean free path. It was found that the hardness and mean free path had a linear relationship and significant hardness increases occurred when the mean free path dropped below 100 μm. FSP also significantly enhanced the Al_2O_3 particle dispersion in the coating and yielded low mean free path values. It was also determined that increasing Al_2O_3 content reduced the porosity in the coating, and FSP further lowered the coating porosity due to stirring and compaction effects. The lowest porosity was achieved for the post-FSPed coating containing 35 wt.% Al_2O_3.

It was found that the tensile properties, such as UTS, failure strain and coating toughness for the as-sprayed Al_2O_3 coatings improved with increasing Al_2O_3 content. The strength and elongation enhancement with increasing Al_2O_3 content for the as-sprayed coatings was mainly attributed to the reduction of physical defects, such as porosity in the coating. The improvement in Al_2O_3 particle dispersion also contributed to the strengthening of the coatings. The as-sprayed coatings yielded very small elongations due to the embrittled nature of cold sprayed MMC coatings. Following FSP, the coatings experienced strength improvements with remarkable gains in the coating elongation and toughness. The failure strain and toughness for the post-FSPed

coatings increased by an order of magnitude compared to the as-sprayed coatings. The coating with the highest UTS was the post-FSPed coating containing 35 wt.% Al_2O_3 with a UTS of 172 MPa. The enhanced elongation and ductility of the coatings following FSP was attributed to the dynamic recrystallization that occurs during FSP. It was concluded that the microstructural changes due to dynamic recrystallization enhanced the ductility of the coatings, without compromising the coating tensile strength. The as-sprayed coating fracture surface presented a brittle fracture highlighting the weak interparticle bonding between the Al matrix. The recrystallization was evident on the fracture surfaces of the post-FSPed samples, which presented a dimpled rupture and ductile failure mode with an abundance of large and deep dimples. It was also determined that physical defects, such as porosity, dominate the tensile performance of the coatings and overshadow the strength improvements from microstructural enhancement. Coatings with 35 wt.% Al_2O_3 exhibited significant improvements in tensile properties, as their porosity was below 1%, allowing for microstructural enhancements to further improve the tensile performance.

Lastly, it was determined that FSP also enhanced the wear performance of the coatings, yielding lower wear rates for post-FSPed coatings. It was also found that coatings with greater Al_2O_3 content exhibited improved wear rates. The enhanced wear performance following FSP was attributed to the reduced porosity and improved Al_2O_3 dispersion in the coating. The study concluded that cold sprayed and FSPed Al-Al_2O_3 MMC coatings can be used to repair unrepairable, cold-worked Al alloys such as AA 5052-H32 with minimal strength losses in the base material. Therefore, the novel cold spray-FSP hybrid fabrication approach can be used to effectively perform geometric and functional repairs for cold-worked Al alloys.

6. FUTURE WORK AND RECOMMENDATIONS

The focus of this study was to assess the feasibility of a novel technique for developing coatings using low-pressure cold spray and FSP to repair unrepairable, cold worked Al alloys. Cold sprayed Al-Al_2O_3 MMC coatings were fabricated and FSP was performed on them with the aim of performing functional and geometric repairs for AA5052-H32. To characterize the mechanical performance of the coatings before and after FSP, several tests were performed including hardness testing, uniaxial tensile testing, and abrasion testing. This study was designed to lay the groundwork for future studies to expand on the feasibility of using cold spray and FSP to develop coatings with enhanced mechanical properties to eventually develop a novel hybrid cold spray-FSP fabrication system where both processes occur simultaneously.

To further the work done in this study, several additional tests may be performed to further understand the performance of this repair methodology. Adhesion testing for the coatings may be performed as per ASTM C633 [64] to quantify the adhesion strength of the coatings on the base material. Although the coatings fabricated as part of this study did not experience delamination during any of the tests, it is important to ensure that the coatings will not peel off in other applications. Preliminary tests were conducted for the as-sprayed coating samples, however testing of the post-FSPed samples needs to be performed to further understand the effects of FSP on the coating-substrate interface. The results from the preliminary tests are illustrated in Figure 29.

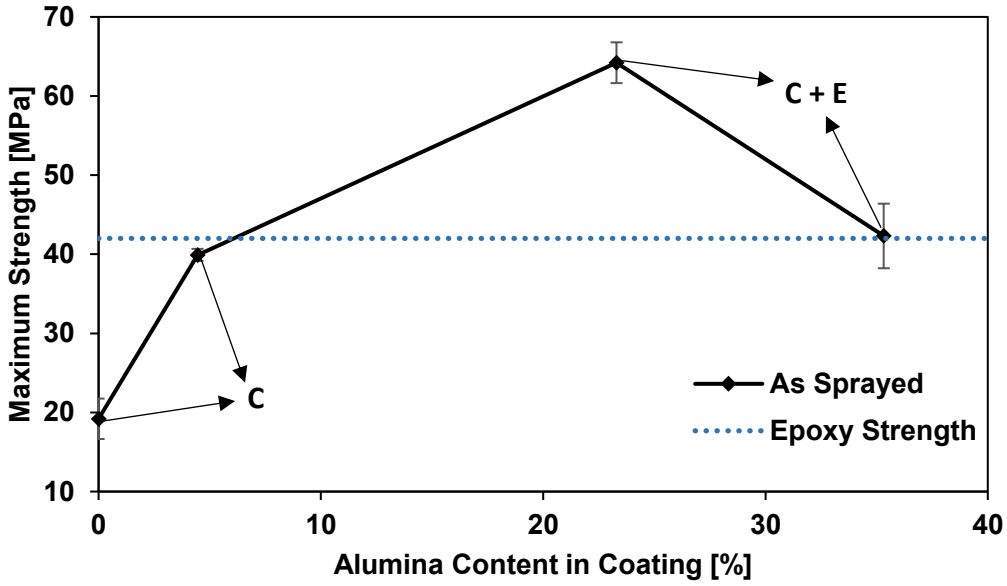

Figure 29: Preliminary adhesion testing as per ASTM C633 for the as-sprayed coatings. On the figure, C indicates cohesive failure in the coating and E indicates failure in the epoxy section.

Since FSP is capable of introducing strength reduction into AA5052-H32, the interface of the coating with the base material becomes a region of interest for potential strength losses. Though tensile testing of stand-alone coating samples has been performed for this study, in order to understand the behaviour of the coating-substrate interface, tensile testing of the coating and substrate assembly can be performed. Using DIC in tandem with the tensile testing and analyzing the coating-substrate interface as it is projected to a tensile loading may allow to further the understanding of the effects of FSP and cold spray on the base material. To mitigate the minor thermal softening experienced by the 35 wt.% Al_2O_3 coatings following FSP, performing under water FSP can also be considered. Under water FSP would allow lowering the heat input of the FSP tool to avoid any thermal defects and softening in the substrate material.

Since the coatings are being suggested for repairs, it may be important to understand the corrosion resistance of the coatings as they may be used in corrosive environments as is common for the oil/gas industry. Additionally, although the wear rates for the coatings were comparable to cold sprayed coatings fabricated using other materials, surface wear scar and cross-sectional wear scar analysis must be conducted to understand the wear mechanisms and material removal for cold sprayed and FSPed Al-Al_2O_3 coatings. Therefore, SEM imaging of the wear scar must be performed. Using the wear scar analysis, the material removal and wear rates can be related to accepted models.

Though a significant amount of characterization was performed for the as-sprayed and post-FSPed coatings, the grain boundaries in the Al matrix were not analyzed. To understand and quantify the extent of recrystallization in the coating following FSP, it is important to analyze the changes to the grains in the coating matrix. Therefore, it is recommended that Transmission Electron Microscopy (TEM) be performed for the samples to visualize the changes in the grain structure before and after FSP.

To further explore the cold spray-FSP repair methodology, other coating materials can be considered. Specifically, it would be of interest to explore the use of cold sprayed MMC coatings created using powders of heat treatable Al alloys, such as the 2xxx, 6xxx and 7xxx series. Unlike cold worked Al alloys, these alloys allow for increased hardenability through natural ageing after FSP to a T5 temper, potentially leading to improved mechanical and microstructural properties, in particular the wear performance. Therefore, exploring MMC coatings with heat treatable Al alloys as the matrix can be considered to further develop the understanding of cold spray-FSP repairs.

Creating a graded microstructure of cold spray-FSP coating repairs with the Al_2O_3 concentration being higher at the free surface of the repair and lower at the coating-interface

substrate can also be considered to for advanced impact protection. The high concentration of Al_2O_3 will create a high strength region at the free surface of the repair section where impact is likely to occur. The coating-substrate interface, with low Al_2O_3 concentration, will retain more of the Al matrix properties, such as improved elongation and toughness. This strategy can create possibilities for developing application focused repairs.

Lastly, it is important to test the proposed coating repairs on pieces of equipment that will be put into service and exposed to external loading and wear environments. Experimental tests can give an idea of how the coatings will perform and can be used to compare and evaluate different coatings; but field tests subject the coatings to the true environment that can often be difficult to replicate in lab-controlled experiments. Analyzing the failure of the repairs that were performed on parts in service, will allow for deeper insight into the performance and feasibility of this repair methodology.

REFERENCES

[1] D. Rao, K. Huber, J. Heerens, J. F. Santos, and N. Huber, "Materials Science & Engineering A Asymmetric mechanical properties and tensile behaviour prediction of aluminium alloy 5083 friction stir welding joints," *Mater. Sci. Eng. A*, vol. 565, pp. 44–50, 2013, doi: 10.1016/j.msea.2012.12.014.

[2] R. S. Mishra, "Friction stir welding of precipitation strengthened aluminium alloys : scope and challenges Friction stir welding of precipitation strengthened aluminium alloys : scope and challenges," *Sci. Technol. Weld. Join. ISSN*, 2013, doi: 10.1179/1362171811Y.0000000020.

[3] R. A. Behnagh, M. K. B. Givi, and M. Akbari, "Mechanical Properties , Corrosion Resistance , and Microstructural Changes during Friction Stir Processing of 5083 Aluminum Rolled Plates Mechanical Properties , Corrosion Resistance , and Microstructural Changes during Friction Stir Processing of 5083 Al," *Mater. Manuf. Process. ISSN*, 2012, doi: 10.1080/10426914.2011.593243.

[4] A. E. Nolting *et al.*, "Localized Strength Restoration of Aluminum 5083 with Ceramic Particles via Friction Stir Processing," *Proc. NATO-STO AVT-267 Work. Futur. Addit. Manuf. Mil. Hardw.*, pp. 1–18, 2018.

[5] R. S. Mishra, Z. Y. Ma, and I. Charit, "Friction stir processing : a novel technique for fabrication of surface composite," *Mater. Sci. Eng. A341*, vol. 341, no. v, pp. 1–4, 2003.

[6] K. Yang, W. Li, P. Niu, X. Yang, and Y. Xu, "Cold sprayed AA2024/Al2O3 metal matrix composites improved by friction stir processing: Microstructure characterization, mechanical performance and strengthening mechanisms," *J. Alloys Compd.*, vol. 736, pp.

115–123, 2018, doi: 10.1016/j.jallcom.2017.11.132.

[7] F. C. Liu and Z. Y. Ma, “Achieving exceptionally high superplasticity at high strain rates in a micrograined Al-Mg-Sc alloy produced by friction stir processing,” *Scr. Mater.*, vol. 59, no. 8, pp. 882–885, 2008, doi: 10.1016/j.scriptamat.2008.06.035.

[8] I. Charit and R. S. Mishra, “High strain rate superplasticity in a commercial 2024 Al alloy via friction stir processing,” *Mater. Sci. Eng. A*, vol. 359, no. 1–2, pp. 290–296, 2003, doi: 10.1016/S0921-5093(03)00367-8.

[9] M. Weglowski, S. Dymek, and C. Hamilton, “Experimental investigation and modelling of Friction Stir Processing of cast aluminium alloy AlSi9Mg,” *Bull. Polish Acad. Sci. Tech. Sci.*, pp. 893–904, 2013.

[10] Y. T. R. Lee, H. Ashrafizadeh, G. Fisher, and A. McDonald, “Effect of type of reinforcing particles on the deposition efficiency and wear resistance of low-pressure cold-sprayed metal matrix composite coatings,” *Surf. Coatings Technol.*, vol. 324, pp. 190–200, 2017, doi: 10.1016/j.surfcoat.2017.05.057.

[11] A. Moridi, S. M. Hassani-Gangaraj, M. Guagliano, and M. Dao, “Cold spray coating: Review of material systems and future perspectives,” *Surf. Eng.*, vol. 30, no. 6, pp. 369–395, 2014, doi: 10.1179/1743294414Y.0000000270.

[12] A. Sova, A. Papyrin, and I. Smurov, “Influence of ceramic powder size on process of cermet coating formation by cold spray,” *J. Therm. Spray Technol.*, vol. 18, no. 4, pp. 633–641, 2009, doi: 10.1007/s11666-009-9359-5.

[13] R. Ghelichi, S. Bagherifard, M. Guagliano, and M. Verani, “Numerical simulation of cold

spray coating," *Surf. Coatings Technol.*, vol. 205, no. 23–24, pp. 5294–5301, 2011, doi: 10.1016/j.surfcoat.2011.05.038.

[14] A. Papyrin, *The Cold Spray Materials Deposition Process*. Woodhead Publishing Series in Metals and Surface Engineering, 2007.

[15] A. Sova, V. F. Kosarev, A. Papyrin, and I. Smurov, "Effect of ceramic particle velocity on cold spray deposition of metal-ceramic coatings," *J. Therm. Spray Technol.*, vol. 20, no. 1–2, pp. 285–291, 2011, doi: 10.1007/s11666-010-9571-3.

[16] G. Munday, J. Hogan, and A. McDonald, "On the microstructure-dependency of mechanical properties and failure of low-pressure cold-sprayed tungsten carbide-nickel metal matrix composite coatings," *Surf. Coatings Technol.*, 2020, doi: 10.1016/j.surfcoat.2020.125947.

[17] P. Fauchais and G. Montavon, "Thermal and Cold Spray: Recent Developments," *Key Eng. Mater.*, vol. 384, pp. 1–59, 2008.

[18] P. C. King, S. H. Zahiri, and M. Z. Jahedi, "Rare earth/metal composite formation by cold spray," *J. Therm. Spray Technol.*, vol. 17, no. 2, pp. 221–227, 2008, doi: 10.1007/s11666-007-9145-1.

[19] Q. Wang, K. Spencer, N. Birbilis, and M. X. Zhang, "The influence of ceramic particles on bond strength of cold spray composite coatings on AZ91 alloy substrate," *Surf. Coatings Technol.*, vol. 205, no. 1, pp. 50–56, 2010, doi: 10.1016/j.surfcoat.2010.06.008.

[20] K. Hodder, A. Gerlich, J. Villafuerte, and A. McDonald, "Fabrication of aluminum-alumina metal matrix composite coatings via cold gas dynamic spraying at low pressure

followed by friction-stir processing," *Proc. Int. Therm. Spray Conf.*, vol. 556, pp. 231–236, 2012, doi: 10.1016/j.msea.2012.06.066.

[21] T. Peat, A. Galloway, A. Toumpis, P. Mcnutt, and N. Iqbal, "The erosion performance of cold spray deposited metal matrix composite coatings with subsequent friction stir processing," *Appl. Surf. Sci.*, vol. 396, pp. 1635–1648, 2016, doi: 10.1016/j.apsusc.2016.10.156.

[22] S. A. Alidokht, P. Manimunda, P. Vo, S. Yue, and R. R. Chromik, "Cold spray deposition of a Ni-WC composite coating and its dry sliding wear behavior," *Surf. Coatings Technol.*, vol. 308, pp. 424–434, 2016, doi: 10.1016/j.surfcoat.2016.09.089.

[23] A. K. Keshri and A. Agarwal, "Wear Behavior of Plasma-Sprayed Carbon Nanotube-Reinforced Aluminum Oxide Coating in Marine and High-Temperature Environments," *J. Therm. Spray Technol.*, 2011, doi: 10.1007/s11666-011-9669-2.

[24] "'Cold Spray', Thermal Spray Technologies Inc." https://www.tstcoatings.com/ (accessed May 03, 2021).

[25] N. M. Melendez, V. V. Narulkar, G. A. Fisher, and A. G. McDonald, "Effect of reinforcing particles on the wear rate of low-pressure cold-sprayed WC-based MMC coatings," *Wear*, vol. 306, pp. 185–195, 2013, doi: 10.1016/j.wear.2013.08.006.

[26] T. Peat, A. Galloway, A. Toumpis, R. Steel, W. Zhu, and N. Iqbal, "Enhanced erosion performance of cold spray co-deposited AISI316 MMCs modified by friction stir processing," *Mater. Des.*, vol. 120, pp. 22–35, 2017, doi: 10.1016/j.matdes.2017.01.099.

[27] T. W. Gustafson, P. C. Panda, G. Song, and R. Raj, "Influence of Microstructural Scake

on Plastic Flow Behaviour of Metal Matrix Composites," *Acta Mater.*, vol. 45, no. 4, pp. 1633–1643, 1997.

[28] K. Spencer, D. M. Fabijanic, and M. Zhang, "Surface & Coatings Technology The use of Al – Al 2 O 3 cold spray coatings to improve the surface properties of magnesium alloys," *Surf. Coat. Technol.*, vol. 204, no. 3, pp. 336–344, 2009, doi: 10.1016/j.surfcoat.2009.07.032.

[29] A. Loganathan, S. Rengifo, A. F. Hernandez, C. Zhang, and A. Agarwal, "Effect of nanodiamond reinforcement and heat-treatment on microstructure, mechanical and tribological properties of cold sprayed aluminum coating," *Surf. Coatings Technol.*, vol. 412, no. December 2020, p. 127037, 2021, doi: 10.1016/j.surfcoat.2021.127037.

[30] R. F. Vaz, A. Silvello, J. Sanchez, V. Albaladejo, and I. García-Cano, "The influence of the powder characteristics on 316l stainless steel coatings sprayed by cold gas spray," *Coatings*, vol. 11, no. 2, pp. 1–18, 2021, doi: 10.3390/coatings11020168.

[31] X. Zhao, T. Dong, B. Fu, G. Li, Q. Liu, and Y. Li, "Microstructure and properties of cold sprayed nicral coating on az91d magnesium alloy," *Coatings*, vol. 11, no. 2, pp. 1–14, 2021, doi: 10.3390/coatings11020193.

[32] E. Irissou, J. Legoux, B. Arsenault, and C. Moreau, "Investigation of Al-Al 2 O 3 Cold Spray Coating Formation and Properties," *J. Therm. Spray Technol.*, vol. 16, no. December, pp. 661–668, 2007, doi: 10.1007/s11666-007-9086-8.

[33] K. Tsaknopoulos, J. Grubbs, M. Siopis, A. Nardi, and D. Cote, "Microstructure and Mechanical Property Evaluation of Aluminum F357 Powder for Cold Spray Applications," *J. Therm. Spray Technol.*, vol. 30, no. 3, pp. 643–654, 2021, doi:

10.1007/s11666-020-01140-4.

[34] Y. J. Li, X. T. Luo, and C. J. Li, “Improving deposition efficiency and inter-particle bonding of cold sprayed Cu through removing the surficial oxide scale of the feedstock powder,” *Surf. Coatings Technol.*, vol. 407, no. December 2020, p. 126709, 2021, doi: 10.1016/j.surfcoat.2020.126709.

[35] J. Wang, J., Villafuerte, “Low pressure cold spraying of tungsten carbide composite coatings,” *Adv. Mater. Process.*, vol. 167(2), pp. 54–56, 2009.

[36] S. Ahmad Alidokht, P. Vo, S. Yue, and R. R. Chromik, “Erosive wear behavior of Cold-Sprayed Ni-WC composite coating,” *Wear*, vol. 376–377, pp. 566–577, 2017, doi: 10.1016/j.wear.2017.01.052.

[37] S. Dosta, M. Couto, and J. M. Guilemany, “Cold spray deposition of a WC-25Co cermet onto Al7075-T6 and carbon steel substrates,” *Acta Mater.*, vol. 61, no. 2, pp. 643–652, 2013, doi: 10.1016/j.actamat.2012.10.011.

[38] P. Gao, C. Li, G. Yang, Y. Li, and C. Li, “Influence of substrate hardness transition on built-up of nanostructured WC – 12Co by cold spraying,” vol. 256, pp. 2263–2268, 2010, doi: 10.1016/j.apsusc.2009.10.050.

[39] O. Sarikaya, “Effect of some parameters on microstructure and hardness of alumina coatings prepared by the air plasma spraying process,” *Surf. Coatings Technol.*, vol. 190, pp. 388–393, 2005, doi: 10.1016/j.surfcoat.2004.02.007.

[40] L. M. Marzoli, A. Strombeck, and J. F. Dos Santos, “Friction stir welding of an AA6061 / Al2O3/ 20p reinforced alloy,” *Compos. Sci. Technol.*, vol. 66, pp. 363–371, 2005, doi:

10.1016/j.compscitech.2005.04.048.

[41] M. R. Rokni, C. A. Widener, O. C. Ozdemir, and G. A. Crawford, “Microstructure and mechanical properties of cold sprayed 6061 Al in As-sprayed and heat treated condition,” *Surf. Coat. Technol.*, vol. 309, pp. 641–650, 2017, doi: 10.1016/j.surfcoat.2016.12.035.

[42] C. Huang *et al.*, “Modification of a cold sprayed SiCp/Al5056 composite coating by friction stir processing,” *Surf. Coatings Technol.*, vol. 296, pp. 69–75, 2016, doi: 10.1016/j.surfcoat.2016.04.016.

[43] W. Li, Y. Feng, M. P. Planche, H. Liao, and G. Montavon, “Microstructural evolution and mechanical properties enhancement of a cold-sprayed Cu[sbnd]Zn alloy coating with friction stir processing,” *Materials Characterization*, vol. 125. pp. 76–82, 2017, doi: 10.1016/j.matchar.2017.01.027.

[44] G. Munday, “On the Mechanical Properties and Failure of Low-Pressure Cold-Sprayed Tungsten Carbide-Nickel Metal Matrix Composite Coatings,” University of Alberta, 2019.

[45] M. Kouzeli and A. Mortensen, “Size dependent strengthening in particle reinforced aluminium,” *Acta Mater.*, vol. 50, pp. 39–51, 2002.

[46] ASTM International, “G65-16: Standard Test Method for Measuring Abrasion Using the Dry Sand / Rubber Wheel,” *ASTM Stand.*, vol. 04, no. Reapproved 2010, pp. 1–12, 2013, doi: 10.1520/G0065-04R10.2.

[47] ASTM International, “ASTM B611 Standard Test Method for Determining the High Stress Abrasion Resistance of Hard,” *Astm B611*, vol. 13, no. Reapproved 2018, pp. 1–6, 2017, doi: 10.1520/B0611-13.2.

[48] ASTM E8, “ASTM E8/E8M standard test methods for tension testing of metallic materials 1,” *Annu. B. ASTM Stand. 4*, no. C, pp. 1–27, 2010, doi: 10.1520/E0008.

[49] X. T. Luo, G. J. Yang, and C. J. Li, “Multiple strengthening mechanisms of cold-sprayed cBNp/NiCrAl composite coating,” *Surf. Coatings Technol.*, vol. 205, no. 20, pp. 4808–4813, 2011, doi: 10.1016/j.surfcoat.2011.04.065.

[50] C. Q. Huang, J. Deng, S. X. Wang, and L. lei Liu, “A physical-based constitutive model to describe the strain-hardening and dynamic recovery behaviors of 5754 aluminum alloy,” *Mater. Sci. Eng. A*, vol. 699, no. January, pp. 106–113, 2017, doi: 10.1016/j.msea.2017.04.086.

[51] J. Mcclure, “Heat Input and Temperature Distribution in Friction Stir Welding,” *J. Mater. Process. Manuf. Sci.*, no. March 2014, 1998, doi: 10.1106/55TF-PF2G-JBH2-1Q2B.

[52] W. Jinlian, X. Jun, and P. Feng, “Effect of annealing on microstructure and properties of Er modi fi ed 5052 alloy,” *Result Phys.*, vol. 10, no. June, pp. 476–480, 2018, doi: 10.1016/j.rinp.2018.06.048.

[53] R. P. Mahto, C. Gupta, M. Kinjawadekar, A. Meena, and S. K. Pal, “Weldability of AA6061-T6 and AISI 304 by underwater friction stir welding,” *J. Manuf. Process.*, vol. 38, no. January, pp. 370–386, 2019, doi: 10.1016/j.jmapro.2019.01.028.

[54] H. J. Liu, H. J. Zhang, Y. X. Huang, and L. Yu, “Mechanical properties of underwater friction stir welded 2219 aluminum alloy,” *Trans. Nonferrous Met. Soc. China (English Ed.*, vol. 20, no. 8, pp. 1387–1391, 2010, doi: 10.1016/S1003-6326(09)60309-5.

[55] R. Saravanakumar, T. Rajasekaran, and M. Dhanasekaran, “Proceedings Process

parameter optimization in underwater Friction Stir welding of dissimilar aluminium alloy butt joints by design of experiment," *Mater. Today Proc.*, no. xxxx, 2021, doi: 10.1016/j.matpr.2021.05.283.

[56] K. Holmberg, A. Laukkanen, E. Turunen, and T. Laitinen, "Wear resistance optimisation of composite coatings by computational microstructural modelling," *Surf. Coatings Technol.*, vol. 247, pp. 1–13, 2014, doi: 10.1016/j.surfcoat.2014.02.019.

[57] A. A. Torrance, "Modelling abrasive wear," *Wear*, vol. 258, no. 1-4 SPEC. ISS., pp. 281–293, 2005, doi: 10.1016/j.wear.2004.09.065.

[58] N. Chawla and K. K. Chawla, "Microstructure-based modeling of the deformation behavior of particle reinforced metal matrix composites," *J. Mater. Sci.*, vol. 41, no. 3, pp. 913–925, 2006, doi: 10.1007/s10853-006-6572-1.

[59] Z. H. Zhang, W. Y. Li, Y. Feng, J. L. Li, and Y. J. Chao, "Global anisotropic response of friction stir welded 2024 aluminum sheets," *Acta Mater.*, vol. 92, pp. 117–125, 2015, doi: 10.1016/j.actamat.2015.03.054.

[60] A. Mansur, "Modeling of Mechanical Properties of Ceramic-Metal Composites for Armor Applications," 2011.

[61] X. Xie *et al.*, "Achieving simultaneously improved tensile strength and ductility of a nano-TiB2/AlSi10Mg composite produced by cold spray additive manufacturing," *Compos. Part B Eng.*, vol. 202, no. September, p. 108404, 2020, doi: 10.1016/j.compositesb.2020.108404.

[62] C. Shao, C. Lo, K. Bhagavathula, A. McDonald, and J. Hogan, "High strength particulate

aluminum matrix composite design: Synergistic strengthening strategy," *Compos. Commun.*, vol. 25, no. February, 2021, doi: 10.1016/j.coco.2021.100697.

[63] U. F. Kocks and H. Mecking, "Physics and phenomenology of strain hardening: the FCC case U.F.," *Prog. Mater. Sci.*, vol. 48, pp. 171–273, 2002.

[64] ASTM International, "ASTM C633 - 13 Standard Test Method for Adhesion or Cohesion Strength of Thermal Spray Coatings," vol. 13, no. Reapproved 2017, pp. 1–8, 1993, doi: 10.1520/C0633-13R17.1.

[65] M. S. Corporation, "Intelligent Stir Welding for Industry and Research (ISTIR) Process Development System (PDS)."

APPENDIX A – STRESS STRAIN CURVES

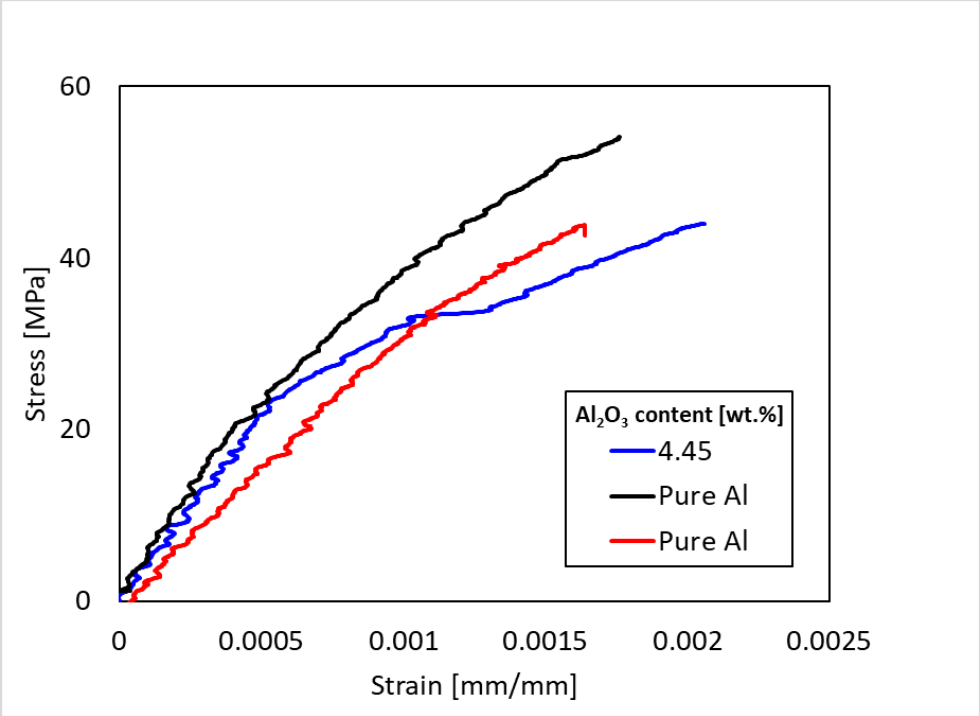

Figure 30: Stress strain curves for the as-sprayed pure Al and 5 wt.% Al_2O_3 coatings.

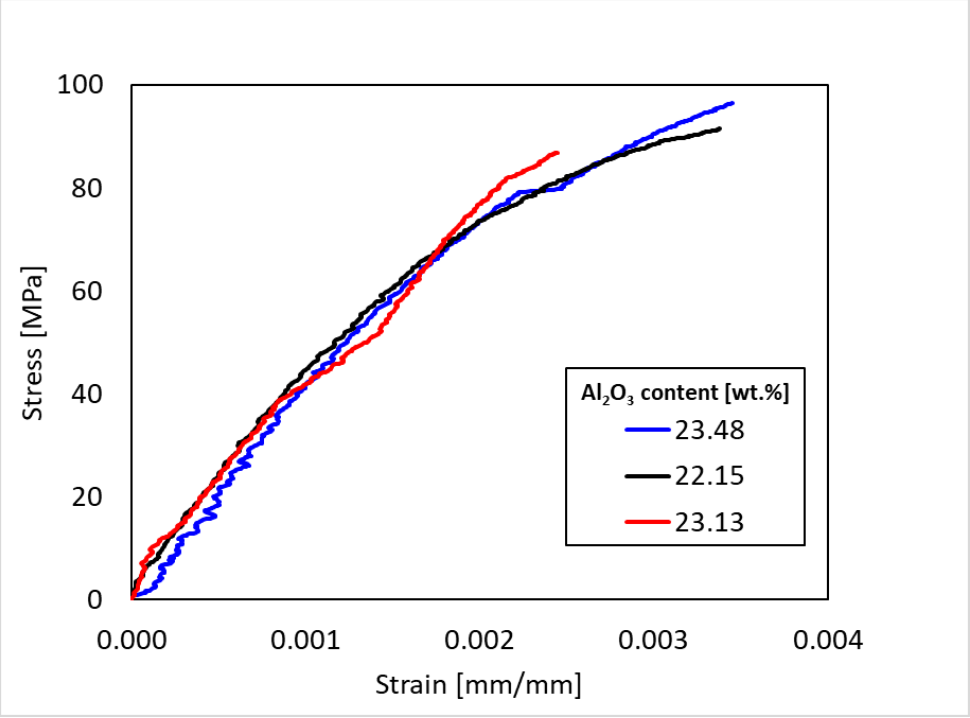

Figure 31: Stress strain curves for the as-sprayed coatings containing 23 wt.% Al_2O_3.

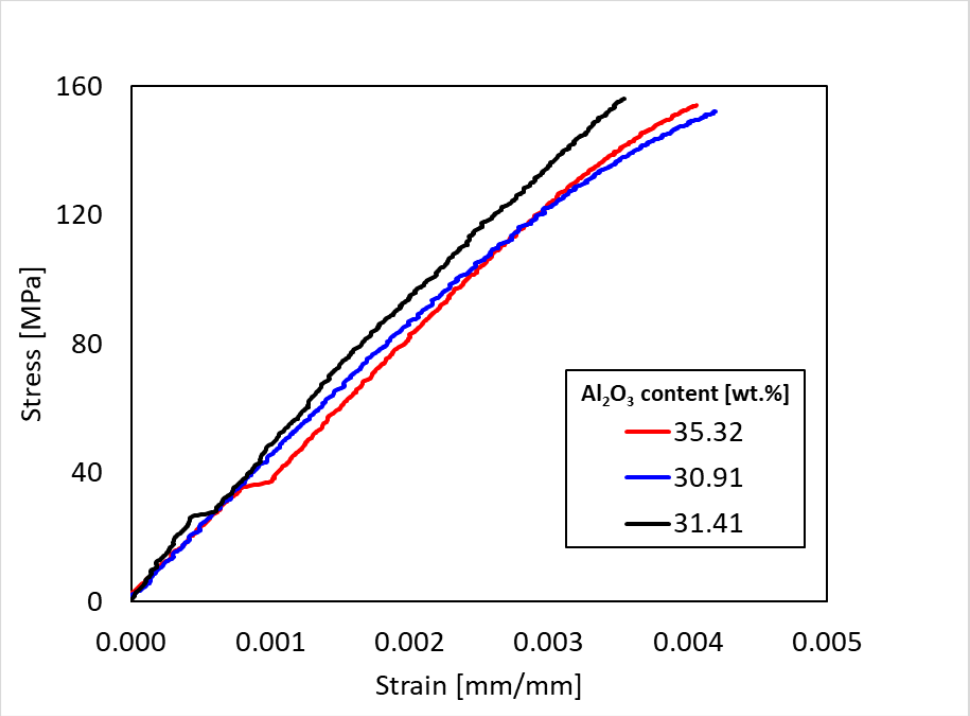

Figure 32: Stress strain curves for the as-sprayed coatings containing 35 wt.% Al_2O_3.

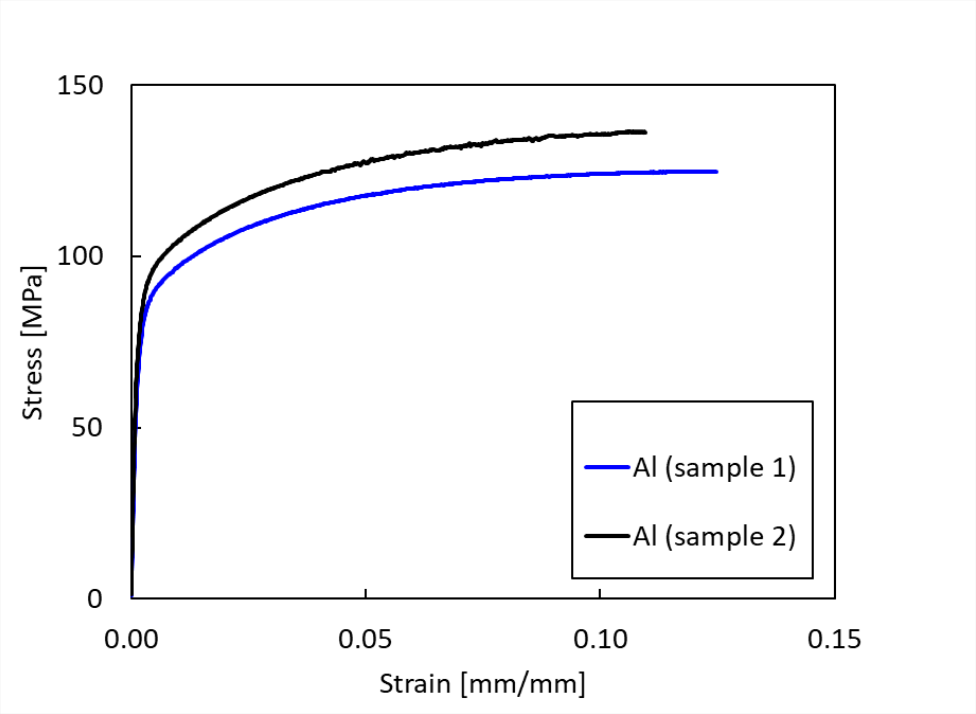

Figure 33: Stress strain curves for the post-FSPed pure Al coatings.

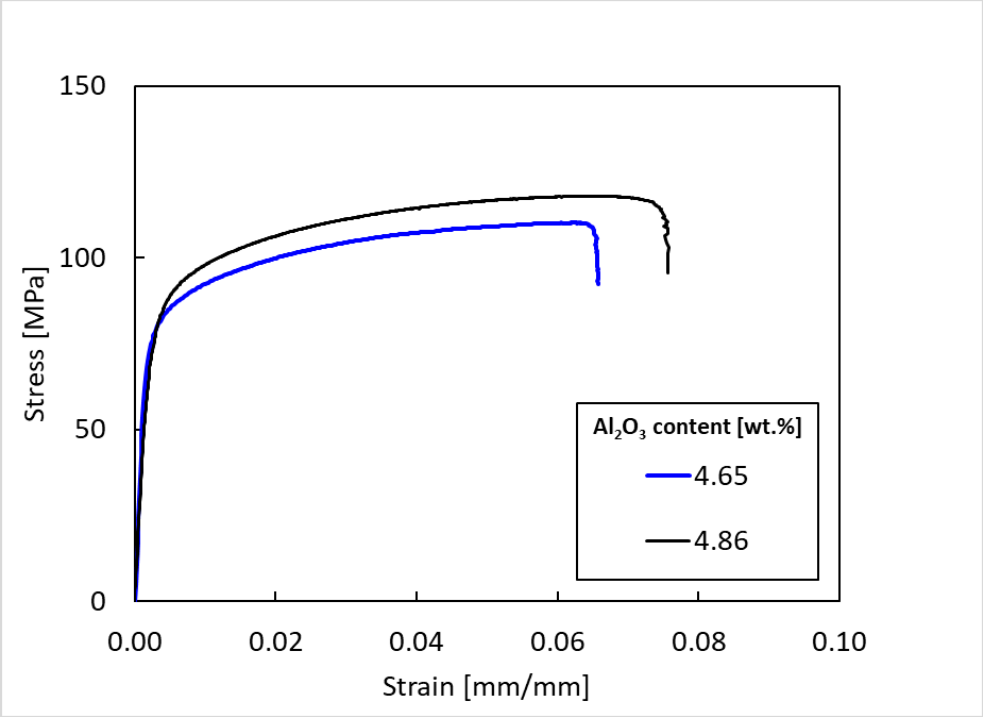

Figure 34: Stress strain curves for the post-FSPed coatings with 5 wt.% Al_2O_3.

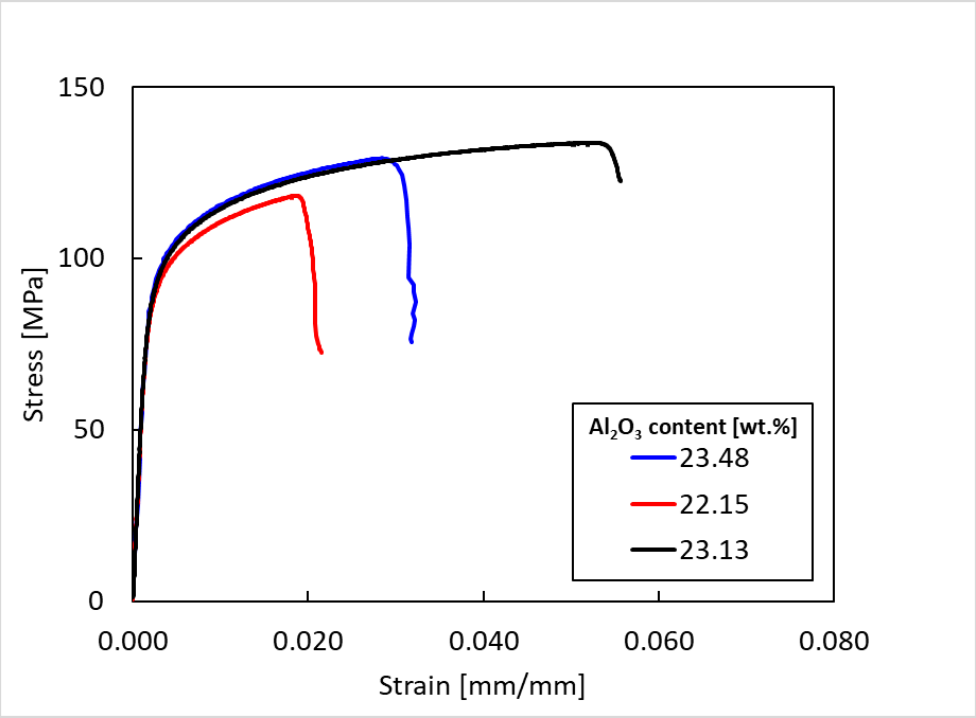

Figure 35: Stress strain curves for the post-FSPed coatings with 23 wt.% Al_2O_3.

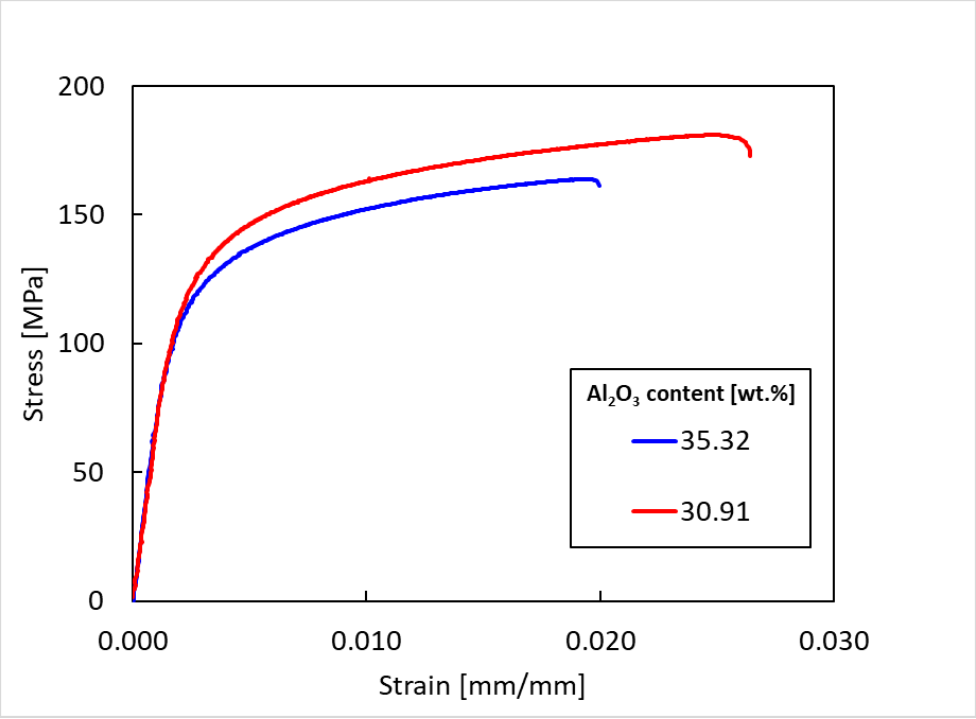

Figure 36: Stress strain curves for the post-FSPed coatings with 35 wt.% Al_2O_3.